Membrane fission during bacterial spore development requires DNA-pumping driven cellular inflation

Ane Landajuela[1,2†*], Martha Braun[2,3†*], Alejandro Martínez-Calvo[4,5], Christopher D. A. Rodrigues[6], Carolina Gomis Perez[1,2], Thierry Doan[7], David Z. Rudner[8], Ned S. Wingreen[9,10], Erdem Karatekin[1,2,3,11*]

1 Cellular and Molecular Physiology, Yale University, New Haven, CT, USA

2 Nanobiology Institute, Yale University, West Haven, CT, USA

3 Molecular Biophysics and Biochemistry, Yale University, New Haven, CT, USA

4 Princeton Center for Theoretical Science, Princeton University, Princeton, NJ 08544, USA

5 Department of Chemical and Biological Engineering, Princeton University, Princeton, NJ 08544, USA

6 iThree Institute, University of Technology Sydney (UTS), Australia

7 Laboratoire d'Ingénierie des Systèmes Macromoléculaires, Aix-Marseille Université - CNRS UMR7255, Marseilles, France

8 Department of Microbiology, Harvard Medical School, Boston, Massachusetts,USA

9 Department of Molecular Biology, Princeton University, Princeton, NJ 08544, USA.

10 Lewis-Sigler Institute for Integrative Genomics, Princeton University, Princeton, NJ 08544, USA.

11 Université de Paris, SPPIN - Saints-Pères Paris Institute for the Neurosciences, Centre National de la Recherche Scientifique (CNRS), F-75006 Paris, France.

† These authors contributed equally

* To whom correspondence should be addressed

ane.landajuela@yale.edu

matha.braun@yale.edu

erdem.karatekin@yale.edu (lead contact)

SUMMARY

Bacteria require membrane fission for cell division and endospore formation. FisB catalyzes membrane fission during sporulation, but the molecular basis is unclear as it cannot remodel membranes by itself. Sporulation initiates with an asymmetric division that generates a large mother cell and a smaller forespore that contains only 1/4 of its complete genome. As the mother cell membranes engulf the forespore, a DNA translocase pumps the rest of the chromosome into the small forespore compartment, inflating it due to increased turgor. When the engulfing membranes undergo fission, the forespore is released into the mother cell cytoplasm. Here we show that forespore inflation and FisB accumulation are both required for efficient membrane fission. We suggest that high membrane tension in the engulfment membrane caused by forespore inflation drives FisB-catalyzed membrane fission. Collectively our data indicate that DNA-translocation has a previously unappreciated second function in energizing FisB-mediated membrane fission under energy-limited conditions.

HIGHLIGHTS

- Membrane fission during endospore formation requires rapid forespore inflation by ATP-driven DNA translocation.
- Forespore inflation is fast enough to increase the tension of the engulfment and forespore membranes to near lysis tensions.
- FisB catalyzes membrane fission by impeding the flux of lipids that partially support forespore and engulfment membrane growth.
- Membrane fission utilizes chemical energy transduced to mechanical energy during DNA-packing into the forespore.

INTRODUCTION

When nutrients are scarce, spore-forming bacteria initiate a morphological process called sporulation, which produces dormant, stress-resistant spores that can remain dormant for many years until conditions are favorable for germination (Moir and Cooper, 2015; Setlow, 2003). The first morphological event during sporulation is the formation of an asymmetric septum that produces a small forespore and a larger mother cell (Figure 1A). The mother cell membranes then engulf the forespore in a process reminiscent of phagocytosis. When the edges of the engulfing membrane reach the cell pole, they undergo membrane fission to release the forespore (Figure 1A inset), now surrounded by two membranes, into the mother-cell cytoplasm. The mother cell then packages the forespore in a protective cortex and coat while the forespore prepares for dormancy. When the forespore is mature, the mother cell lyses, releasing the dormant spore into the environment. Before asymmetric division, the chromosomes are remodeled into an axial filament with the origins of replication at the cell poles and the termini at the mid-cell (Webb et al., 1997). Thus, immediately after asymmetric division, only ~1/4 of the forespore chromosome is trapped inside the forespore (Wu and Errington, 1994, 1998). The rest of the chromosome is pumped into the forespore by an ATPase, SpoIIIE (Bath et al., 2000; Wu and Errington, 1997), consuming one ATP molecule per every two base pairs translocated (Liu et al., 2015). As the chromosome is packed into the forespore, the forespore volume doubles from its initial volume of $\sim 0.1\ \mu m^3$ by the time the engulfment membrane migrates completely around the forespore and continues to grow to $\sim 0.3\ \mu m^3$ about 3 h after septation (Lopez-Garrido et al., 2018). Forespore inflation is driven by osmotic forces which are mainly due to the counterions that are needed to neutralize the highly charged DNA (Lopez-Garrido et al., 2018). Upon complete DNA packing, the pressure difference between the forespore and mother cell reaches ~60 kPa (Lopez-Garrido et al., 2018). It has been suggested that DNA translocation can be seen as an energy transduction process, converting the chemical energy stored in ~1.5 million ATP molecules to mechanical energy, stretching the thin peptidoglycan layer between the forespore and engulfment membranes and smoothing their wrinkles (Lopez-Garrido et al., 2018). However, it is not clear if this stored mechanical energy is ever utilized by the nutrient-deprived, sporulating bacteria, and if so, how.

Here, we investigate the relationship between forespore inflation driven by DNA translocation and the membrane fission event that releases the forespore into the mother cell cytoplasm. We previously showed that this event is catalyzed by the protein FisB that accumulates at the neck of the engulfing membranes during sporulation in *Bacillus subtilis* (Doan et al., 2013; Landajuela et al., 2021). FisB, a ~250 residue protein that is conserved among endospore-forming bacteria, is produced after asymmetric division in the mother cell (Doan et al., 2013). It possesses a short N-terminal cytoplasmic domain, a single-pass transmembrane domain (TMD), and a large extracytoplasmic domain (ECD, Figure 1B) (Landajuela et al., 2021). In cells lacking FisB (*ΔfisB*), engulfment proceeds normally, but the membrane fission step is impaired (Doan et al., 2013; Landajuela et al., 2021). Membrane fission can be assessed during a sporulation time course by labeling cells with a lipophilic dye that crosses the cell membrane inefficiently (Figure 1C). In cells that have not yet undergone fission, the dye has access to the forespore, engulfing, and mother cell membranes, resulting in a

stronger signal where these three membranes are in close proximity. By contrast, in cells that have undergone membrane fission, the dye only weakly labels the internal membranes, allowing the quantification of cells that have undergone fission at a given time point after initiation of sporulation (Landajuela et al., 2021) (Figure 1D). A functional GFP-FisB fusion forms dim mobile clusters (DMC), each containing ~12 GFP-FisB molecules. An intense spot at the engulfment pole (ISEP) containing ~40 copies of GFP-FisB appears around the time of membrane fission (Figure 1E,F and (Landajuela et al., 2021)). FisB localizes to the membrane neck that connects the engulfment membrane to the rest of the mother cell membrane based only on lipid-binding, self-aggregation, and the unique geometry encountered at the end of engulfment (Landajuela et al., 2021). FisB self-oligomerizes and binds acidic lipids, bridging artificial membranes, but does not appear to have other binding partners. During sporulation, the only location where FisB can bridge membranes is at the membrane neck that eventually undergoes membrane fission (Figure 1F), suggesting homo-oligomerization and trans interactions that bridge membranes are sufficient to explain FisB accumulation in the neck during late stages of engulfment (Landajuela et al., 2021). However, how membrane fission occurs at the last step of engulfment is not known.

Here we show that forespore inflation and FisB accumulation at the membrane neck are both required for efficient membrane fission. Interventions that slowed or prevented forespore area expansion delayed or inhibited membrane fission, even when FisB had accumulated at the membrane neck. Conversely, sporulating cells lacking FisB had impaired membrane fission but their forespores expanded. We find that membrane fission is driven by the combination of high tension in the engulfment membrane due to forespore inflation and FisB oligomerization impeding lipid flux that partially supports forespore and engulfment membrane growth. Our results demonstrate that part of the mechanical energy stored during the process of DNA packaging into the forespore is used for membrane fission.

RESULTS

FisB does not remodel membranes, but forms a stable, extended network on GUV membranes

The simplest mechanism of FisB-catalyzed membrane fission would involve direct membrane remodeling by FisB, similar to eukaryotic membrane fission machineries dynamin (Ferguson and De Camilli, 2012) or ESCRT-III (Schoneberg et al., 2017). To test this idea, we studied interactions of the FisB extracellular domain (ECD) with model GUV membranes. We fluorescently labeled recombinant purified FisB ECD with iFluor555-maleimide at a cysteine introduced at residue 123 (iFluor-FisB ECD, Figure 2A), a substitution that does not affect FisB's function (Landajuela et al., 2021). GUV membranes were labeled by including a fluorescent lipid in the lipid composition. Membranes and the labeled protein were then visualized using spinning-disc confocal (SDC) microscopy (Figure 2). We first incubated GUVs with various concentrations of iFluor-FisB ECD in a closed chamber for 60 min, then imaged the membranes and FisB ECD (Figure 2B). iFluor-FisB ECD did not bind GUVs lacking acidic lipids, as reported previously (Landajuela et al., 2021). By contrast, iFluor-FisB ECD bound GUVs

140 containing 30 mole % cardiolipin (CL). At 20 nM in solution, FisB binding to GUVs was
141 barely detectable, but at ~75 nM, discrete FisB spots were visible. These spots diffused
142 around the GUV membrane, reminiscent of the DMC in live cells. At 200 nM and above,
143 most GUVs were covered more uniformly and completely by iFluor-FisB ECD.
144 Consistent with previous work (Landajuela et al., 2021), and unlike many proteins
145 implicated in eukaryotic membrane fission (Campelo and Malhotra, 2012; Renard et al.,
146 2018; Simunovic et al., 2019), FisB did not cause any membrane deformations such as
147 tubulation or invaginations. Because such deformations are opposed by membrane
148 tension, we repeated these experiments using deflated GUVs with lower membrane
149 tension. Even at high coverage and when the GUVs were deflated, FisB did not cause
150 any remodeling of GUV membranes (Figure 2B). However, we noticed that deflated
151 GUVs covered with iFluor-FisB ECD did not display shape fluctuations typical of bare
152 deflated GUVs, suggesting FisB may form a fixed, extended network on the membranes
153 stabilizing the membrane shape.

154 We reasoned that if FisB ECD does indeed form an extended network on membranes,
155 its mobility should be low in such regions. To test this, we performed fluorescence
156 recovery after photobleaching (FRAP) experiments (Figure 2C). We incubated 1 μM
157 iFluor-FisB ECD with GUVs for 2 h. This allowed for a range of iFluor-FisB ECD
158 coverage of GUVs. Some GUVs were uniformly covered by iFluor-FisB ECD whereas
159 some others were covered only partially by iFluor-FisB ECD patches. We bleached the
160 iFluor-FisB ECD fluorescence in a rectangular region of interest (ROI) and monitored
161 the subsequent recovery on a given GUV. Recovery was faster for GUVs that had
162 partial, patchy iFluor-FisB ECD coverage, as new patches diffused into the bleached
163 region (Figure 2C upper row and Figure 2D). By contrast, there was virtually no
164 recovery for GUVs that were uniformly covered by iFluor-FisB ECD (Figure 2C lower
165 row and Figure 2D). To relate FisB ECD membrane coverage to mobility, we plotted the
166 mean iFluor-FisB ECD signal along the contour of the GUV, $F_{\mathrm{mean}}^{\mathrm{ECD}}$, against the fractional
167 fluorescence recovery 45 s after bleaching, as shown in Figure 2E. This analysis
168 showed that increasing FisB ECD coverage led to decreased FisB ECD mobility,
169 consistent with the idea that FisB ECD forms a denser, less dynamic network as
170 coverage increases.

171 To test how stable the FisB ECD network is, we dissolved the membranes after the
172 network had formed while observing iFluor-FisB ECD signals. Five to ten minutes after
173 addition of Triton X-100 the lipid signal disappeared, suggesting that the membranes
174 were dissolved. Remarkably, iFluor-FisB ECD signals were intact (Figure 2F), indicating
175 that once formed, the three-dimensional FisB ECD network was stable even after the
176 removal of the membrane.

177 Altogether, these data argue that FisB does not remodel membranes but is capable of
178 forming an extended, stable network in which individual FisB molecules are immobile.

179

180 **Forespore inflation accompanies membrane fission**

181 How can FisB catalyze membrane fission if it cannot remodel membranes by itself? We
182 reasoned that an additional cellular process should be involved, given that direct
183 interactions with other proteins could not be detected (Doan et al., 2013; Landajuela et

al., 2021). A process that could potentially influence membrane fission is the forespore volume increase that occurs after asymmetric division due to translocation of DNA into the forespore by the ATPase SpoIIIE (Lopez-Garrido et al., 2018) (Figure 3A). However, whether and how this volume increase is related to membrane fission was not known. We began by investigating whether there was a correlation between forespore inflation and membrane fission. We used the lipophilic fluorescent dye 1-(4-trimethylammoniumphenyl)-6-phenyl-1,3,5-hexatriene p-toluenesulfonate (TMA-DPH) that allowed us to detect forespore contours of both cells that had undergone membrane fission and those that had not (Landajuela et al., 2021). We used a semi-automated active-contour fitting algorithm (Smith et al., 2010) and estimated the membrane areas from the surface of revolution around the long axis of symmetry (Methods). Three hours after initiation of sporulation via nutrient downshift, post-fission forespores were visually larger than their remaining pre-fission counterparts (Figure 3B). The average areas of pre- and post-fission forespores decreased and increased as a function of time after the nutrient downshift, respectively (Figure 3C), suggesting cells with rapidly growing forespores underwent membrane fission, leaving behind smaller pre-fission forespores. Similar trends were obtained using a soluble CFP forespore marker (Figure S1), ruling out potential artifacts due to the use of a lipophilic membrane dye. The close link between forespore inflation and membrane fission was even more evident when we plotted the percentage of cells having undergone membrane fission against the post-fission forespore area, which yielded a nearly linear relationship (Figure 3D).

The forespore area difference between pre- and post-fission cells, ΔA_{FS}, increased during sporulation to reach 1.3 ± 0.1 μm^2 (Figure 3E). Taking into account the 4 membrane leaflets that must grow together and assuming an area per lipid of $\sim 0.7\ \mathrm{nm}^2$, $\sim 7.4 \times 10^6$ new lipids must be added to the engulfment and forespore membranes during sporulation. Given that this growth occurs over ~2 h, lipids must be added at an average rate of ~1,000 lipids/s to the forespore and engulfment membranes. Interestingly, vegetative cell membrane areas grow at a comparable rate ($\dot{A}_{\mathrm{veg}} = 0.020\ \mu\mathrm{m}^2/\mathrm{min}$, or about ~1000 lipids/s, taking into account two leaflets, 95% confidence interval: 0.007-0.023 μm^2/min, n=8 cells), consistent with the finding that phospholipid synthesis during sporulation occurs near the maximal rate associated with vegetative growth (Pedrido et al., 2013). Thus, forespore inflation requires high rates of *de novo* phospholipid synthesis despite energy-limiting conditions, and most of the newly synthesized lipids are utilized for forespore area growth during the late stages of engulfment and after fission.

In summary, there is a clear correlation between membrane fission at the end of engulfment and forespore inflation, suggesting that forespore growth may facilitate membrane fission.

Hypothesis: increasing membrane tension during forespore inflation drives FisB-dependent membrane fission

How can forespore inflation promote FisB-mediated membrane fission? We hypothesized that increased membrane tension due to forespore inflation, coupled with

228 FisB oligomerization at the membrane neck, could work synergistically to drive
229 membrane fission. Because DNA pumping into the forespore leads to forespore inflation
230 through increased turgor, and smooths membrane wrinkles (Lopez-Garrido et al., 2018),
231 there must be an associated increase in the tension of the forespore membrane.
232 Furthermore, because the forespore and engulfment membranes are separated through
233 a thin layer of peptidoglycan only ~20 nm wide (Khanna et al., 2019; Tocheva et al.,
234 2011), we expect the tension and the area of the engulfment membrane (which
235 eventually undergoes fission) to increase together with that of the forespore membrane.
236 The membrane tension of the forespore and engulfment membranes can be estimated
237 from the excess osmotic pressure in the forespore, ~60 kPa (Lopez-Garrido et al.,
238 2018). Assuming the two membranes that surround the forespore balance the excess
239 osmotic pressure, then according to Laplace's Law $\Delta P = 4\gamma/R_{\mathrm{fs}}$, so that a forespore
240 radius of $R_{\mathrm{fs}} = 400$ nm implies a membrane tension $\gamma \sim 6$ pN nm^{-1}. This is a very high
241 value, around values expected for membrane rupture (Evans et al., 2003; Needham and
242 Nunn, 1990; Ojkic et al., 2014). It is thus likely that the peptidoglycan cell wall
243 surrounding the forespore may actually be necessary during forespore inflation to avoid
244 membrane rupture (Lopez-Garrido et al., 2018).

245 The hypothesis that increasing membrane tension during forespore inflation drives FisB-
246 dependent membrane fission leads to the following predictions. First, interfering with
247 forespore inflation should hinder membrane fission. Even when forespore inflation is
248 slowed or blocked, FisB should be able to properly localize to the membrane neck
249 (provided engulfment is not compromised), because FisB's localization relies solely on
250 its interactions with itself and with membranes, and the geometry of the neck
251 (Landajuela et al., 2021). Second, in the absence of FisB, forespores should inflate but
252 membrane fission should be impaired.

253

254 **Blocking lipid synthesis impedes forespore inflation and membrane fission**

255 Lipid synthesis is required during vegetative growth (Yao et al., 2012; Zhang and Rock,
256 2008) and sporulation (Pedrido et al., 2013; Schujman et al., 1998) and fatty acid
257 availability determines average cell size (Vadia et al., 2017). When *B. subtilis* cells are
258 placed in a nutrient poor medium, lipid synthesis is initially downregulated, but with the
259 onset of sporulation, it returns close to the maximal rate (Pedrido et al., 2013). We
260 reasoned that blocking lipid synthesis at different time points after the initiation of
261 sporulation should block forespore area expansion at different stages. Furthermore, if
262 forespore inflation is needed for membrane fission, the percentage of forespores
263 blocked in inflation should correlate with those stalled at the pre-fission stage.

264 We blocked the synthesis of neutral lipids and phospholipids at different time points t
265 after nutrient downshift using cerulenin, a drug that inhibits *de novo* fatty acid
266 biosynthesis (Heath and Rock, 2004) (Figure S2A). We then probed the cells for
267 membrane fission at $t = 3$ h using TMA-DPH labeling. We found that the earlier lipid
268 synthesis was blocked, the smaller the fraction of cells that had undergone membrane
269 fission at $t = 3$ h (Figure S2B,C). Both pre-and post-fission forespore membrane areas
270 decreased with longer cerulenin application (Figure S2D). These results are consistent
271 with previous reports that *de novo* lipid synthesis is needed for engulfment and

272 forespore inflation (Lopez-Garrido et al., 2018; Pedrido et al., 2013). In addition to
273 perturbing engulfment (Figure S2E,F) FisB accumulation at the fission site was reduced
274 in the presence of cerulenin (Figure S2G), making it difficult to infer the role of forespore
275 inflation in membrane fission. In order to unmask the contribution of forespore inflation
276 on membrane fission, we focused on cells in which FisB had successfully accumulated
277 at the membrane fission site. We discovered that an increasing fraction of these cells
278 failed to undergo membrane fission with longer cerulenin application (Figure S2H).
279 Thus, although impaired engulfment and FisB accumulation at the fission site partially
280 account for the membrane fission defects observed, blocking lipid synthesis inhibited
281 membrane fission even for cells with proper FisB localization, suggesting forespore
282 inflation facilitates membrane fission.

283

284 **Slowing DNA translocation slows membrane fission**

285 In addition to lipid synthesis, forespore inflation requires ATP-dependent DNA
286 translocation into the forespore. Accordingly, in a complementary set of experiments we
287 took advantage of previously characterized mutations in the DNA translocase SpoIIIE to
288 investigate whether forespore inflation contributes to membrane fission.

289 We began by using an ATPase mutant (SpoIIIE36) that is translocation defective
290 (Pogliano et al., 1997). In the absence of DNA pumping, the forespores remained small
291 and engulfment was severely perturbed (Figure S3A), similar to the engulfment
292 phenotype of the Δ*spoIIIE* mutant reported previously (Doan et al., 2013). Membrane
293 fission was severely impaired in these cells (Figure S3B) as was forespore area growth,
294 both for pre-fission and the small number of post-fission forespores (Figure S3C). The
295 fission defect can only be partly explained by deficient FisB localization, as 23±4 % of
296 the SpoIIIE36 cells had an ISEP at 3 h after the nutrient downshift, compared to 70±6%
297 of WT cells (Figure S3G), yet only 5% of the SpoIIIE36 cells had undergone membrane
298 fission at this timepoint (Figure S3B). Importantly, among cells with an ISEP at the end
299 of engulfment, only ~16±4% of SpoIIIE36 cells had undergone membrane fission
300 compared to ~91±6% % of WT cells (Figure S3H). This difference was even more
301 pronounced when we used a sensitized background in which FisB was expressed at ~8-
302 fold lower levels than wild-type (Doan et al., 2013; Landajuela et al., 2021). Under these
303 conditions, there were no post-fission SpoIIIE36 cells at hour 3 of sporulation among the
304 7% that had an ISEP. By contrast, 95% of the sporulating cells with SpoIIIE^{WT} that had
305 an ISEP had undergone membrane fission in this FisB low-expression background
306 (Figure S3G,H). Altogether, these results suggest that membrane fission requires both
307 FisB accumulation at the neck (ISEP formation) and forespore inflation.

308 The severe engulfment defects in the SpoIIIE36 mutant have the potential to obscure
309 the contribution of forespore inflation to FisB localization and membrane fission.
310 Accordingly, we took advantage of a second mutant (SpoIIIE^{D584A}) that translocates
311 DNA ~2.5-fold slower than wild-type (Burton et al., 2007) and does not have engulfment
312 defects (Figure 4). In sporulating cells expressing *spoIIIE*^{D584A}, forespore inflation was
313 delayed for post-fission cells and the average forespore area of the remaining pre-
314 fission cells increased instead of decreasing as for wild-type cells, suggesting slow

315 forespore inflation slows membrane fission (Figure 4A-C). This was more evident when
316 the percentage of cells that had undergone fission was plotted together with the post-
317 fission forespore areas as functions of time (Figure 4D). The percentage of cells that
318 underwent membrane fission increased with the increase in post-fission forespore area
319 (Figure 4E). Importantly, engulfment (Figure 4F,G) and FisB localization (Figure 4H)
320 were similar to wild-type. In fact, by hour 3 of sporulation, *spoIIIE*^{D584A} cells accumulated
321 ~1.4-fold more FisB at the cell pole than did wild-type cells (Figure 4I), yet only ~40% of
322 the *spoIIIE*^{D584A} cells had undergone membrane fission compared to ~75% of the wild
323 type cells (Figure 4D), demonstrating that accumulating more FisB does not necessarily
324 lead to more efficient membrane fission.

325 Together, these results strongly suggest that FisB accumulation at the membrane neck
326 is *not* a sufficient condition for membrane fission; fission additionally requires forespore
327 enlargement.

328

329 **In the absence of FisB, forespores inflate but fission is impaired**

330 Our data suggest that FisB accumulation at the fission site and forespore inflation work
331 together to drive membrane fission. To investigate whether these two processes occur
332 independently, we monitored forespore membrane area changes in cells expressing
333 FisB at low levels or altogether lacking it.

334 We analyzed forespore area at different time points after a nutrient downshift, using
335 TMA-DPH (Figure 5). As anticipated, most sporulating cells lacking FisB (*ΔfisB*) did not
336 undergo membrane fission (Figure 1D) despite completing engulfment (Figure 5A)
337 (Doan et al., 2013; Landajuela et al., 2021). Remarkably, the forespore areas of these
338 pre-fission cells, $A_{\mathrm{FS}}^{\mathrm{pre}}$, increased as a function of time after the nutrient downshift, nearly
339 doubling by $t = 3.5$ h, while those of wild-type cells decreased slightly during the same
340 period (Figure 5B). The forespore areas of the small fraction of *ΔfisB* cells that
341 underwent membrane fission (Figure 1), $A_{\mathrm{FS}}^{\mathrm{post}}$, were slightly larger than those of wild-
342 type cells and followed a similar time course, increasing as a function of time (Figure
343 5C).

344 Sporulating cells expressing GFP-FisB at ~8-fold lower levels than wild-type undergo
345 membrane fission more slowly (Figure S4). In these cells, post-fission forespore areas,
346 $A_{\mathrm{FS}}^{\mathrm{post}}$, were slightly larger than those expressing GFP-FisB at native levels, and in both
347 cases $A_{\mathrm{FS}}^{\mathrm{post}}$ increased over time (Figure S4F). Similar to the Δ*fisB* mutant, the pre-
348 fission forespore area increased as a function of time when GFP-FisB levels were
349 reduced albeit the increase was more modest (Figure S4E).

350 Overall, these results indicate that forespore inflation occurs independently of FisB, but
351 that forespore inflation is not sufficient to catalyze efficient membrane fission. When
352 FisB is present, the fission process is greatly accelerated by forming an aggregate at
353 the membrane neck to be severed, but only if the forespore is inflating (Figure 5D).

354

Modeling suggests increased engulfment membrane tension is the primary driver of FisB-catalyzed membrane fission

Next, we modeled the effect of increased membrane tension on membrane neck geometry, including the roles of hydrodynamic drag on the forespore due the DNA pumping and the osmotic pressure difference between the cytoplasm and the lumen of the neck. We developed a minimal model based on free energy minimization, considering the free energy F of an axisymmetric and mirror symmetric membrane neck connecting two membrane sheets, corresponding to the local geometry of the neck formed between the forespore and mother cell membranes (see SI Appendix for details). The energy functional F consists of a term accounting for membrane bending and tension, F_{m}, another term, F_p, accounting for an osmotic pressure difference $\Delta p = p_{\mathrm{cyto}} - p_{\mathrm{peri}}$ between the cytoplasm and periplasm since the lumen of the neck is continuous with the periplasmic space, and finally a term representing any pulling force f on the forespore, e.g. due to DNA translocation, F_f.

We first explored the role of membrane tension, γ, on neck geometry. As shown previously (Landajuela et al., 2021) using a minimal model for the neck as a cylinder of radius r_{cyl} and length L_{cyl}, there are two regimes: (1) For a large neck (radius larger than a critical radius r_{crit}), membrane tension drives the neck to become ever larger. (2) By contrast, for an initial $r_{\mathrm{cyl}} < r_{\mathrm{crit}}$, the neck will relax to a finite equilibrium radius set by the balance between membrane tension and membrane bending stiffness. Intuitively, these two regimes follow because as the radius of the cylindrical neck grows, the area of the cylinder grows $\sim L_{\mathrm{cyl}}\, r_{\mathrm{cyl}}$, but the areas of the associated flat membranes on the mother cell and forespore *shrink* $\sim r_{\mathrm{cyl}}^2$. While the former term can dominate for small r_{cyl} leading to a local minimum, the latter term eventually dominates for large r_{cyl} implying the neck will open. The existence of a local minimum of neck radius is recapitulated by this simplified model in SI Appendix Eqs. 1 and 5. As seen in SI Appendix Fig. 2a, in regime (2) increasing membrane tension γ results in a narrowing of the equilibrium neck radius. While to our knowledge there has been no direct measurement of the membrane tension in *B. subtilis*, we find that reasonable values of $\gamma = 0.1 - 1$ pN nm^{-1} are sufficient to achieve a neck radius < 10 nm (Ojkic et al., 2014). It is likely that cell wall remodeling that drives engulfment (Ojkic et al., 2016) brings the neck radius into regime (2), because a neck forms and a small fraction of cells undergo membrane fission even in the absence of FisB (Figure 1 and Figure 5).

To examine the additional role of osmotic pressure difference between the cytoplasm and the lumen of the neck, we also minimized F at finite Δp. While $\Delta p = 0.1$ atm has little effect on the neck radius, $\Delta p = 0.6$ atm, which is realistic for *B. subtilis* (Lopez-Garrido et al., 2018; Ojkic et al., 2014) further reduces the minimum neck radius, by e.g. ~1 nm (SI Appendix Fig. 2b and 5), for a fixed value of the membrane tension, $\gamma = 0.84$ pN nm^{-1}. This reduction makes sense, as higher osmotic pressure in the mother cell will tend to compress the volume of the periplasmic space contained within the neck.

By contrast, a pulling force on the forespore not only stretches the neck but also *increases* its equilibrium radius (see SI Appendix Fig. 5). A pulling force of $f = 50 -$

398 100 pN, around the maximum force that can be applied by one or two SpoIIIE motors
399 translocating DNA into the forespore (Allemand and Maier, 2009; Liu et al., 2018) (see
400 SI Appendix for more details), increases the minimum neck radius significantly
401 compared to a case where there is no pulling force. In particular, the membrane neck
402 radius increases by $\sim 4\ \mathrm{nm}$, when $f = 100$ pN, considering $\Delta p = 0, \gamma = 0.84$ pN nm^{-1}
403 (SI Appendix Fig. 5a). One can understand this effect simply by considering the total
404 force in the neck at the midpoint, which is the product of the circumference of the neck
405 times the membrane tension, $f = 2\pi r_{\mathrm{min}}\gamma$. So at fixed membrane tension γ, an increase
406 of the pulling force f automatically implies an increasing r_{min}. Moreover, an osmotic
407 pressure difference of $\Delta p = 0.6$ atm is able to reduce the minimum neck radius by ~1
408 nm even if the pulling force f is not zero, as shown in SI Appendix Fig. 5b, for a fixed
409 value of the membrane tension $\gamma = 0.84$ pN nm^{-1}.

410 It is likely that the membrane tension in the rapidly expanding forespore and engulfment
411 membranes is higher than in the mother cell membrane. We estimated an upper limit for
412 this membrane tension gradient, by estimating the gradient that would be sufficient to
413 drive a flux of lipids in the neck matching the observed average increase in forespore
414 membrane area (see above and SI Appendix). Perhaps surprisingly, the resulting
415 difference is only $\sim 10^{-7}$ pN nm^{-1}, which is orders of magnitude less than the expected
416 overall membrane tension. Thus an unimpeded flux of lipids between the mother cell
417 and forespore will have negligible effect on the equilibrium results presented above.
418 However, if this flux is strongly impeded, e.g. by accumulation of FisB at the neck, the
419 tension in the engulfment membrane around the forespore would increase further,
420 possibly contributing to membrane fission (see below).

421 In summary, modeling suggests that the pulling force on the forespore exerted by DNA
422 translocation has a negligible effect on neck geometry. By contrast, a realistically high
423 membrane tension, possibly augmented by an osmotic pressure difference across the
424 membrane, is sufficient to drive the equilibrium neck radius down to ≤ 5-10 nm, with two
425 expected consequences. First, with a small neck radius, FisB can interact in *trans* and
426 accumulate in the neck, facilitating membrane fission (Landajuela et al., 2021). Second,
427 high membrane tension and a small neck radius likely both facilitate membrane fission.

428

429 **Membrane fission catalyzed by FisB-lipid friction under high membrane tension**

430 Our results so far suggest that increased membrane tension due to forespore inflation
431 drives FisB-catalyzed membrane fission. Increased membrane tension in the
432 engulfment membrane would provide a driving force for membrane flow from the mother
433 cell to the engulfment membrane through the neck connecting the two compartments.
434 One possibility is that by forming an oligomer at the membrane neck, FisB impedes the
435 movement of lipids that partially support this growth, further increasing the tension in the
436 engulfment membrane, promoting membrane fission. To test this possibility, here we
437 studied lipid flows between membrane compartments in live cells and how lipid mobility
438 is affected by FisB oligomerization.

439 We first tested if FisB oligomerization on a membrane can impede lipid movement. We
440 incubated FisB ECD with GUVs labeled with fluorescent Cy5-lipids, allowing FisB ECD

to form a dense scaffold as in Figure 2. We then probed lipid mobility using FRAP as shown in Figure 6. In the absence of FisB ECD, fluorescence of the bleached region recovered rapidly and nearly completely, indicating unimpeded diffusion, as expected. However, when GUVs were coated with FisB ECD, about half the lipids became immobile (Figure 6C). We conclude that FisB oligomerization severely impedes lipid mobility.

Next, we tested if forespore inflation leads to membrane movement between the mother cell and engulfment membrane compartments. We followed the kinetics of forespore area growth in individual cells and related the kinetics to membrane fission. Using time-lapse microscopy, we imaged individual sporulating cells labeled with the lipophilic dye FM4-64 (Lopez-Garrido et al., 2018) as shown in Figure 6D,E (see Figure S5 for more examples). While TMA-DPH crosses the cell membrane slowly, FM4-64 does not cross it, which allowed us to detect the time of membrane fission in addition to monitoring membrane areas. The non-fluorescent FM4-64 molecules in the aqueous phase exchange with the membrane-inserted fluorescent ones (Cochilla et al., 1999). Membrane fission isolates the small inter-membrane space from the bath, blocking exchange of bleached dyes with unbleached ones in the bath and accelerating decay of the fluorescence signals arising from the forespore and engulfment membranes. A plot of forespore contour fluorescence as a function of time for individual cells shows a stable signal, which starts decreasing upon membrane fission. We cross-correlated these individual fluorescence profiles with a model decay function to determine the timing of membrane fission (Figure 6F). We defined $t = 0$ as the frame just preceding fission (Figure 6E,F) and aligned all measurements with respect to this time before averaging membrane areas as shown in Figure 6G,H. The rate of forespore area increase slowed gradually after membrane fission (Figure 6G). Remarkably, the mother cell area shrank before and grew after membrane fission (Figure 6H).

Until FisB accumulates at the membrane neck and the membrane undergoes fission, there are two sources of lipids to support the growth of the forespore and engulfment membranes: *de novo* lipid synthesis and lipid flux between the mother cell and engulfment membranes (Figure 6I). After membrane fission, substantial expansion of the forespore and engulfment membranes can only be supported by *de novo* lipid synthesis. Thus, analysis of the rates of area changes can be informative about lipid flux through the neck. We focused on the mother cell area changes for this analysis, because the lipid synthesis rate in the forespore likely increases as a function of time as the lipid synthase genes are gradually translocated into the forespore (Pedrido et al., 2013). The mother cell area changed at rates of $-0.011\ \mu\mathrm{m}^2/\mathrm{min}$ (-262 lipids/s) and $+0.0032\ \mu\mathrm{m}^2/\mathrm{min}$ (+76 lipids/s) before and after fission, respectively. Assuming the rates of insertion into the mother cell of newly synthesized lipids pre- and post-fission do not change appreciably, we estimate ~340 lipids/s move through the neck toward the engulfment membrane before FisB accumulation – a significant fraction of the maximal cellular lipid synthesis capacity (see above). Membranes lyse when stretched above only ~1 % in area (Evans et al., 2003). Hence, assuming that the total area of the engulfment and forespore membranes is ~ 5 $\mu\mathrm{m}^2$, a deficit of ~300 lipids/s would cause a 1% deficit of the membrane area, i.e. ~ 0.05 $\mu\mathrm{m}^2$, within ~ 4 min if the area expanded at fixed number of lipids. Thus, it is possible that FisB oligomerization – by interfering

with lipid flux through the neck – leads to a further increase in the engulfment membrane tension and thus facilitates membrane fission.

DISCUSSION

Bacteria rely on membrane fission for every division cycle and during endospore formation. FisB is the only molecule described so far with a dedicated role in membrane fission in bacteria (Doan et al., 2013; Landajuela et al., 2021), but how FisB catalyzes membrane fission has remained unclear. Here we report that FisB does not remodel membranes directly but forms a stable network on them. Thus, another cellular process must be involved to achieve membrane fission at the end of engulfment. Surprisingly, we found that pumping of the chromosomal DNA into the forespore by the ATPase SpoIIIE – a seemingly unrelated process – is a necessary condition for FisB-dependent membrane fission. DNA pumping into the forespore leads to forespore inflation through increased turgor, stretching the thin layer of peptidoglycan between the forespore and engulfment membranes and smoothing membrane wrinkles (Lopez-Garrido et al., 2018). FisB accumulation at the membrane fission site and forespore inflation are both necessary conditions for efficient membrane fission.

We propose that increased membrane tension in the engulfment membrane due to forespore inflation drives membrane fission (Figure 7). High membrane tension can cause membrane fission through opening of a transient pore (Karatekin et al., 2003), as was shown for fission catalyzed by BAR domain proteins scaffolding a membrane tube under extension (Simunovic et al., 2017). The presence of a protein scaffold on a membrane tube has a dual role: slowing equilibration of membrane tension by impeding membrane flow, and acting as a heterogeneous nucleation point for a membrane defect, lowering the energy barrier for membrane poration (Simunovic et al., 2017). Thus, FisB can similarly have a dual role in membrane fission. First, by oligomerizing at the membrane neck, FisB impedes membrane flow from the mother cell membrane to the engulfment membrane where tension is higher, leading to a further increase in tension, making fission more likely. Second, the FisB oligomer-bare membrane interface could provide a nucleation point for a membrane defect at high tension.

Membrane fission requires energy input. For all biological membrane fission reactions described to date, membrane fission is energized and regulated locally. For the best characterized cases, membrane fission proteins dynamin (Ferguson and De Camilli, 2012) or ESCRT III (Schoneberg et al., 2017) polymerize at the membrane fission site and use the energy liberated by nucleoside triphosphate hydrolysis to reshape membranes locally. By contrast, here we have found that membrane fission during endospore formation in *B. subtilis* is energized indirectly through DNA translocation into the forespore – a process that is required primarily for genetic inheritance and at first sight bears little relation to the membrane fission that occurs at the opposite end of the engulfment membrane. This situation is analogous to secondary transporters using electrochemical gradients set by primary pumps such as the sodium-potassium ATPase to energize secondary transport processes (Boron and Boulpaep, 2017).

Additionally, our results clarify the role of SpoIIIE in membrane fission during endospore

formation. It was originally proposed that in addition to DNA translocation, SpoIIIE drives membrane fission because an ATPase deficient mutant resulted in membrane fission defects (Liu et al., 2006; Sharp and Pogliano, 1999). However, SpoIIIE's role in membrane fission remained unclear because the knock-out or ATPase dead mutants (Figure S3 and (Doan et al., 2013)) cause severe engulfment defects. Since FisB localization and membrane fission occur downstream of engulfment, any engulfment defect would also lead to defects in FisB localization and membrane fission and would not be particularly informative about membrane fission itself. Here we establish that SpoIIIE does indeed play a critical role in membrane fission even in the absence of engulfment defects, but this role is related to forespore inflation.

The membrane fission mechanism we have described here provides an elegant example of how bacteria can use energy very efficiently under starvation conditions. DNA translocation into the forespore is an energy-consuming process that cannot be bypassed, but the byproduct of this process, namely increased turgor in the forespore, can be harnessed to energize secondary processes. It will be interesting to see if processes other than membrane fission are energized by mechanical energy stored in the inflated forespore.

ACKNOWLEDGEMENTS

We thank all members of the Karatekin laboratory for fruitful discussions and Jeorg Nikolaus (director of the Yale West Campus Imaging Core) for help with imaging. This work was supported by National Institute of General Medical Sciences and National Institute of Neurological Disorders and Stroke of the National Institutes of Health (NIH) under award numbers R01GM114513 and R01NS113236 (to EK). The content is solely the responsibility of the authors and does not necessarily represent the official views of the National Institutes of Health. This work was supported in part by the National Science Foundation, through the Center for the Physics of Biological Function (PHY-1734030) and was performed in part at the Aspen Center for Physics, which is supported by National Science Foundation grant PHY-1607611. AMC also acknowledges support from the Princeton Center for Theoretical Science and the Human Frontier Science Program through the grant LT000035/2021-C. We gratefully acknowledge a Yale University Predoctoral Fellowship to MB.

AUTHOR CONTRIBUTIONS

EK, MB, AL, and DZR conceived the study. MB carried out most of the experiments with purified proteins and artificial membranes, AL carried out live cell imaging and analysis. AL and CGP performed the lipid mobility measurements. MB, EK wrote matlab scripts for image analysis, AL, MB analysed images. AMC and NSW developed the mathematical model, DZR, NSW and EK supervised the work. CDAR and TD provided reagents and intellectual input. EK wrote the manuscript, with input from all authors.

CONFLICT OF INTEREST

The authors declare they have no conflicts of interest.

573 **FIGURE LEGENDS**

574 **Figure 1. FisB is required for efficient membrane fission during sporulation**. **A.**
575 Schematic of sporulation stages. Upon starvation, sporulation is initiated by asymmetric
576 division into a mother cell (MC) and a forespore (FS). The MC then engulf the FS. At the
577 end of engulfment, a thin neck or tube connects the engulfment membrane to the rest of
578 the MC membrane (red box). Fission of the neck releases the FS, now surrounded by
579 two membranes, into the MC cytoplasm. Upon maturation, the FS turns into a spore and
580 the MC lyses to release it. Inset: membrane fission step marking the end of engulfment.
581 **B**. Domain structure of FisB (Doan et al., 2013; Landajuela et al., 2021). **C**. Membrane
582 fission assay. An aliquot of cells is labeled with the lipophilic dye 1-(4-
583 trimethylammoniumphenyl)-6-phenyl-1,3,5-hexatriene p-toluenesulfonate (TMA-DPH)
584 which fluoresces only once inserted into the membrane. The dye labels internal
585 membranes poorly. If a cell has not yet undergone membrane fission at the time of
586 TMA-DPH labeling, the dye has access to the space between the engulfment and FS
587 membranes, resulting in brighter labeling of the MC, FS, and engulfment membranes
588 when these are adjacent to one another (top row). After fission, the dye labels internal
589 membranes poorly (bottom row). **D**. Time course of membrane fission for wild-type
590 cells, *ΔfisB* cells, or *ΔfisB* cells complemented with mGFP-FisB expressed at native
591 levels (strain BAM003). Some membrane fission occurs even in the absence of FisB
592 (*ΔfisB*, gray markers). Mean±SEM from 3 independent experiments are shown (>300
593 cells were analyzed per point). **E.** Wide-field fluorescence microscopy images of cells
594 expressing mGFP-FisB at native levels (strain BAM003). Aliquots were taken from the
595 suspension at indicated times after nutrient downshift, labeled with TMA-DPH, and
596 images of mGFP-FisB and membranes were acquired sequentially. Examples of
597 sporulating cells with mGFP-FisB enriched at the septum (1.5 h), forming a dim mobile
598 cluster (DMC; 2.5 h) and with a discrete mGFP-FisB focus at the cell pole (intense spot
599 at engulfment pole, ISEP, 3 h) are highlighted with arrowheads. Scale bars represent
600 1μm. **F**. Schematic of FisB dynamics (Landajuela et al., 2021). At the end of
601 engulfment, ~40 FisB molecules accumulate at the neck into an immobile cluster to
602 catalyze membrane fission.

603 **Figure 2. FisB does not remodel membranes. A**. The soluble recombinant fragment
604 of FisB comprising its extracytoplasmic domain (ECD) used in the experiments with
605 GUVs. **B**. Interactions of FisB ECD with GUV membranes ("100% PC" and "30% CL"
606 membranes are composed of (all mole %) 99 PC, 1 NBD-PE, and 30 *E. coli* CL, 69
607 eggPC, 1 NBD-PE, respectively). At low concentrations, FisB ECD forms small mobile
608 clusters. With increasing concentration, labeling becomes more uniform. Even at high
609 coverage or with deflated GUVs (right), no membrane remodeling is evident (deflated
610 GUVs were composed of (all mole %) 25 *E. coli* PE, 5 *E. coli* CL, 50 *E. coli* PG, 19
611 eggPC and 1 DiD or NBD-PE (BS mix)). **C**. Mobility of FisB ECD decreases with
612 increasing coverage. GUVs composed of BS mix were incubated with 1 μM iFluor555-
613 FisB ECD for 2h. GUVs were covered with protein to varying degrees. Top row shows
614 fluorescence recovery of a GUV with low iFluor555-FisB ECD coverage. Bottom row
615 shows an example of a GUV fully covered with iFluor555-FisB ECD fluorescence that
616 does not recover after photobleaching. Photobleached regions are indicated with boxes.
617 **D**. Normalized fluorescence intensity from the boxed regions in C as a function of time.

618 **E**. Higher protein coverage (∝ mean GUV membrane intensity) leads to lower protein
619 mobility. The fractional fluorescence recovery 45 s post-bleaching ($(F_{45} - F_0)/(1 - F_0)$,
620 where F_{45} is the fluorescence intensity at 45 s and F_0 is the intensity just after bleaching,
621 both relative to pre-bleach intensity) is plotted as a function of mean GUV membrane
622 intensity. Each dot represents a GUV. **F**. FisB ECD forms a fixed, stable network on the
623 GUV membrane that persists even after the membranes are dissolved with detergent. 1
624 μM iFluor555-FisB ECD was incubated with deflated GUVs for 2h, then Triton X-100
625 was added (1.7 mM final concentration, 7-8-fold above the critical micelle concentration
626 (Tiller et al., 1984)), and the sample imaged 5-10 min thereafter.

627 **Figure 3. Forespore area increase during sporulation correlates with membrane**
628 **fission activity. A**. Schematic of SpoIIIE-mediated pumping of the chromosome into
629 the forespore leading to forespore inflation. **B**. Images show wild-type strain (PY79) at
630 *t*=3 h after nutrient downshift to initiate sporulation. Membranes were visualized using
631 TMA-DPH. Forespores of cells that have undergone membrane fission (red contours on
632 the right panel) are larger than those that have not yet undergone membrane fission
633 (blue contours). Scale bars represent 1 μm. **C**. Quantification of forespore membrane
634 area for cells that have (red, "post") or have not (blue, "pre") undergone membrane
635 fission. **D**. The percentage of cells that have undergone membrane fission as a function
636 of post-fission forespore area. **E**. The difference between post- and pre-fission
637 forespore areas, ΔA_{FS}, grows as a function of time. In C-E, mean±SEM of 3
638 independent experiments are shown, with 70 cells analyzed per data point.

639 **Figure 4. Slower forespore inflation leads to slower membrane fission with no**
640 **adverse effect on engulfment or FisB localization. A**. Fluorescence microscopy
641 images of TMA-DPH labeled wild-type SpoIIIE strain BAL039 (top row, times after
642 nutrient downshift are indicated). The lower row shows the same images, but with the
643 overlaid forespore contours for cells that have (red) or have not (blue) undergone
644 membrane fission. **B.** As in A, but for the slow DNA-pumping SpoIIIE strain BAL040
645 (SpoIIE^{D584A}). **C**. The average forespore area for pre- (blue) and post-fission (red) cells
646 as a function of time into sporulation for the SpoIIE^{D584A} (dashed lines, strain BAL040)
647 or wild-type (solid lines) cells (strain BAL039). (n=25-70 cells per data point). **D**. The
648 percentage of cells that have undergone membrane fission (left axis, black) followed a
649 very similar time course as the forespore area as a function of time (right axis, magenta)
650 for both WT (solid lines) and SpoIIE^{D584A} (dashed lines) cells. Both membrane fission
651 and forespore inflation were delayed in SpoIIE^{D584A} cells (>300 cells per data point). **E**.
652 The percentage of post-fission cells increased with increasing forespore area for both
653 WT (black) and SpoIIE^{D584A} (magenta) cells. WT data is copied from Figure 3 for
654 comparison. **F.** Fluorescence microscopy images of WT or SpoIIE^{D584A} cells expressing
655 mGFP-FisB at native levels in a *ΔfisB* background, probed 3h after the nutrient
656 downshift. Membranes were labeled with TMA-DPH. In cells expressing WT SpoIIIE
657 (top row) post-fission cells have larger forespores (red contours) and FisB is
658 accumulated at the membrane fission site (red arrowheads). At this stage, most cells
659 expressing SpoIIE^{D584A} are still in the pre-fission stage, even if engulfment is visually
660 complete and FisB has accumulated at the membrane fission site. **G.** Percentage of WT
661 or SpoIIE^{D584A} cells with engulfment membrane migration completed by t=3 h into
662 sporulation. Engulfment is not perturbed significantly by the slow DNA pumping by

663 SpoIIE^{D584A} (>300 cells per data point). **H**. FisB localization is not perturbed in
664 SpoIIE^{D584A} cells compared to WT cells. **I**. Distributions of mGFP-FisB fluorescence
665 intensities for the ISEP in willd-type ("WT") and the slow DNA pumping by SpoIIE^{D584A}
666 mutant strain ("slow"). Representative regions of interest (and regions taken for
667 background correction, "Bg") are shown on the example images on the left. The means
668 ($\pm$ SD) are 70 ± 17 a.u. for WT and 99 ± 18 for SpoIIE^{D584A} ISEP intensities. Since for
669 WT this intensity corresponds to ~40 copies of FisB (Landajuela et al., 2021), we
670 conclude that nearly 60 copies are accumulated in SpoIIE^{D584A}. Scale bars represent 1
671 μm in A, B, and F. Means$\pm$SEM for 3 biological replicates are plotted in panels C-E,
672 G,H. See Figure S3 for results with an ATPase dead SpoIIIE mutant.

673 **Figure 5**. **In the absence of FisB, forespores inflate but fission is impaired. A**.
674 Representative images of wild-type (PY79) or *ΔfisB* cells (BDR1083) at the indicated
675 times after nutrient downshift. Membranes were visualized with TMA-DPH. Lower
676 panels show the FS contours for cells that have (red) or have not (blue) undergone
677 fission. Scale bars represent 1 μm. **B.** The average pre-fission forespore area, $A_{\mathrm{FS}}^{\mathrm{pre}}$,
678 grows during sporulation for *ΔfisB* cells, while it decreases for the wild-type strain. **C**.
679 The average post-fission forespore area, $A_{\mathrm{FS}}^{\mathrm{post}}$, increases faster for *ΔfisB* cells. **D.**
680 Summary of results. FisB catalyzes membrane fission in rapidly growing forespores (top
681 row, "WT rapid inflation"). Slowly inflating forespores are less likely to undergo
682 membrane fission even in the presence of FisB (middle row, "WT slow inflation"). In the
683 absence of FisB, forespores inflate, but fission is rare. See Figure S4 for results with a
684 strain expressing FisB at reduced levels. In B, C, mean$\pm$SEM of 3 independent
685 measurements are shown (70 cells per data point).

686 **Figure 6. FisB impedes lipid diffusion. A-C.** Lipid diffusion is impeded by FisB ECD
687 oligomerization on membranes. **A**. Schematic of the experiment. A region of interest (2
688 μm by 2 μm by ~1 μm in xyz) is bleached and fluorescence recovery is monitored for
689 bare GUVs or GUVs covered by FisB ECD labeled with iFluor555. The schematic is
690 drawn from a side view. Actual bleaching and imaging are performed through the
691 bottom. **B**. Snapshots from time-lapse movies at the indicated times for a representative
692 protein-free (top) or a FisB ECD covered GUV (bottom). Time zero corresponds to the
693 frame right after high-intensity bleach. Scale bar is 1 μm. **C**. Quantification of recovery
694 kinetics. To estimate fractional recovery and an approximate recovery time, the
695 corrected and averaged recovery curves were fitted to $f(t) = f_{\infty}(1 - exp(-t/\tau))$ where
696 f_{∞} and τ are the mobile fraction and the recovery timescales, respectively. Best-fit
697 mobile fractions were (with 95% confidence intervals) f_{∞} =0.98 (0.97, 0.99) and 0.48
698 (0.47, 0.49) for bare and FisB ECD coated GUVs, respectively (R^2=0.98-0.99). In both
699 cases $\tau \approx$ 1.7 s, implying a lipid diffusivity of a few $\mu m^2/s$. **D-I.** Membrane flows
700 between membrane compartments before and after membrane fission. **D**. Schematic
701 showing how the timing of membrane fission is detected in time-lapse movies of
702 individual cells. The dye (depicted as a star) becomes highly fluorescent upon insertion
703 into the membrane. The lipid-inserted and free dyes exchange continuously, minimizing
704 bleaching in pre-fission cells. Upon fission, the free dye has no longer access to the
705 inter-membrane space, leading to the onset of an intensity decay. **E.** An example of a
706 single cell, labeled with FM4-64, followed as a function of time (see Figure S5 for more

examples). Top row shows a montage of FM4-64 fluorescence images as a function of time. The middle and bottom rows show the detected forespore and mother cell contours respectively, using an active-contour fitting algorithm. The frame preceding fission is indicated in the image (τ_{fiss}). Bar,1 μm. **F**. Plot of the mean FS contour FM4-64 fluorescence (black) as a function of time for the individual cell in E, displaying a relatively stable signal and a sudden decay upon membrane fission. Cross-correlation of the fluorescence signal with a model decay function (blue) was applied to determine the timing of membrane fission τ_{fiss}. **G**. Average of forespore cell membrane surface area of wild-type sporangia as a function of time (n=25). Time axes for individual cells were aligned such that $\tau_{\text{fiss}} = 0$ min. Error bars represent SEM. The dashed blue and red lines are linear fits to the pre- and fission periods, with slopes 10.6×10^{-3} and $7.9 \times 10^{-3}\ \mu\text{m}^2/\text{min}$. **H**. Similar to G, but for the mother cell areas. The dashed blue and red lines are linear fits to the pre- and fission periods, with slopes -10.5×10^{-3} and $+3.2 \times 10^{-3}\ \mu\text{m}^2/\text{min}$. **I**. Schematic showing sources and sinks of lipids. Before fission, newly synthesized lipids are inserted into the mother cell and engulfment membranes from the mother cell cytoplasm at rates M and S_c, respectively. Lipids synthesized within the forespore are inserted at rate S_f, which likely increases as lipid synthase genes initially located in the mother cell cytopolasm are translocated into the forespore (Pedrido et al., 2013). Lipid flux through the neck (at rate N) is only possible before fission.

Figure 7. Proposed model of how forespore inflation drives FisB-mediated membrane fission. **A**. DNA translocation by the ATPase SpoIIIE inflates the forespore, stretching the thin peptidoglycan layer between two membranes and smoothing membrane wrinkles (Lopez-Garrido et al., 2018). Increased membrane tension in the engulfment membrane drives lipid flux through the neck between the engulfment and mother cell membranes, partially supplying lipids needed for forespore inflation. **B**. FisB oligomerizes at the membrane neck, impeding membrane flow and causing the engulfment membrane to stretch further. **C**. Increased membrane tension drives membrane scission.

736 # STAR★Methods

737

738 ## Key Resources Table

REAGENT or RESOURCE	SOURCE	IDENTIFIER
Chemicals, Peptides, and Recombinant Proteins		
TMA-DPH	Thermo Fisher Scientific	Cat#T204
FM4-64	Thermo Fisher Scientific	Cat#T13320
iFluor™ 555 maleimide	AAT Bioquest	Cat#1063
Cerulenin	Cayman Chemical	Cat# 10005647
Lipids		
Cardiolipin (*E. coli*) (CL)	Avanti Polar Lipids	841199C
L-α-phosphatidylglycerol (*E. coli*) (PG)	Avanti Polar Lipids	841188C
L-α phosphatidylethanolamine (*E. coli*) (PE)	Avanti Polar Lipids	840027C
L-α-phosphatidylcholine (Egg, Chicken) (PC)	Avanti Polar Lipids	840051C
1,2-dioleoyl-sn-glycero-3-phosphoethanolamine-N-(7-nitro-2-1,3-benzoxadiazol-4-yl) (18:1 NBD PE)	Avanti Polar Lipids	810145C
Experimental Models: Organisms/Strains		
Bacillus subtilis PY79	Prototrophic derivative of *B. subtilis* 168	Tax. ID:1415167 (Youngman et al., 1983)
BDR1083	(Doan et al., 2013)	Δ*fisBΩtet*
BKM15	(Doan et al., 2013)	*amyE::PspoIIQ-cfpΩspec*
BDR1066	(Wu and Errington, 1994)	spoIIIEΩneo
BDR1050	(Wu and Errington, 1994)	spoIIIE36
BAT498	(Burton et al., 2007)	*ycgO::PspoIIIE-spoIIIE*D584AΩphleo, spoIIIEΩneo, amyE::PspoIIQ-cfp(Bs) Ωcat*
BAT609		*pelB::PspoIIIE-spoIIIEΩcat*
BAL039	BAT609→ BDR1066 (cat)	spoIIIEΩneo *pelB::PspoIIIE-spoIIIEΩcat*

BAL040	BAT498→ BDR1066 (phleo)	spoIIIEΩneo *ycgO::PspoIIIE-spoIIIE*D584AΩphleo*
BAM003	(Doan et al., 2013)	*ΔfisBΩtet ycgO::PfisB-Mgfp A206K -fisB Ωcat*
BAL003	(Landajuela et al., 2021)	*ΔfisBΩtet, ycgO::PspoIID-RBSfisB(5n)-mGFP A206K-fisBΩerm*
BAL041	BDR1083→ BDR1050(tet)	*ΔfisBΩtet* spoIIIE36
BAL042	pAM002→ BAL041(cat)	*ΔfisBΩtet* spoIIIE36 *ycgO::PfisB-mGFP A206K-fisBΩcat*
BAL043	pAL004→ BAL041(erm)	*ΔfisBΩtet* spoIIIE36 *ycgO::PspoIID-RBSfisB(5n)-mGFP A206K-fisB Ωerm*
BAL044	BDR1083→ BDR1066(tet)	*ΔfisBΩtet* spoIIIEΩneo
BAL045	BAT609 → BAL044(cat)	*ΔfisBΩtet* spoIIIEΩneo *pelB::PspoIIIE-spoIIIEΩcat*
BAL046	BAT498→ BAL044(phleo)	*ΔfisBΩtet* spoIIIEΩneo *ycgO::PspoIIIE-spoIIIE*D584AΩphleo*
BAL047	pAL033→ BAL045 (erm)	*ΔfisBΩtet* spoIIIEΩneo *pelB::PspoIIIE-spoIIIEΩcat yhdG:: PfisB-mGFP A206K -fisB Ωerm*
BAL048	pAL033→ BAL046 (erm)	*ΔfisBΩtet* spoIIIEΩneo *ycgO::PspoIIIE-spoIIIE*D584AΩphleo yhdG:: PfisB-mGFP A206K -fisB Ωerm*
Recombinant DNA		
pKM110		*his6-fisB^{ECD} WT*
pAL007		*his6-fisB^{ECD} WT* G123C
pB034		*yhdGΩerm*
pAM002		*ycgO::PfisB-mGFP -fisBΩcat*
pAM002_IntEcoRImiss		*ycgO::PfisB-mGFP -fisB*No internalEcoRIΩcat*
pAL032		*ycgO::PspoIID-RBSfisB(5n)-mGFP A206K-fisB Ωerm*
pAL032_IntEcoRImiss		*ycgO::PspoIID-RBSfisB(5n)-mGFP A206K-fisB*No internal EcoRIΩerm*

pCB034		yhdGΩerm
pAL033	This work. Built in a two-way ligation with pAM002_IntEcoRImiss cut with EcoRI and BamH1 as insert and pB034 cut with EcoRI and BamH1 as target vector	*yhdG::PfisB-mGFP -fisB Ωerm*
pAL034	This work. Built in a two-way ligation with plasmid pAL032_IntEcoRImiss cut with EcoRI and BamH1 as insert and pB034 cut with EcoRI and BamH1 as target vector	
Oligonucleotides (mutated nucleotides are in bold face)		
oAL001	ctggcgccgctgtg**gca**ggtatgggtttcca	*his6-fisB*^{ECD} G123C
oAL002	tggaaacccatacc**tgc**cacagcggcgcc ag	*his6-fisB*^{ECD} G123C
oAL003	gtcgttaagtttccgttttcatcagg**att**catttg aaacatatctttcatat	FisB T249C
oAL004	atatgaaagatatgtttcaaatg**aat**cctgat gaaaacggaaacttaacgac	FisB T249C
Software and Algorithms		
JFilament	(Smith et al., 2010)	http://athena.physics.lehigh.edu/jfilament/
MatLab	The MathWorks, Inc., Natick, MA	https://www.mathworks.com/

739

740 **Contact for Reagent and Resource Sharing**

741 Further information and requests for resources and reagents should be directed to and
742 will be fulfilled by the Lead Contact, Erdem Karatekin (erdem.karatekin@yale.edu)

743

744 # Method details

745 ## Experimental Procedures

746 **General *B. subtilis* methods**

747 *B. subtilis* strains were derived from the prototrophic strain PY79 (Youngman et al.,
748 1983). Sporulation was induced in liquid medium at 37°C by resuspension according to
749 the method of Sterlini-Mandelstam (Sterlini and Mandelstam, 1969). *B. subtilis* strains
750 were constructed using plasmidic or genomic DNA and a 1-step competence method.
751 Site directed mutagenesis was performed using Agilent's Quick-change Lightning kit

752 following manufacturer's instructions and mutations were confirmed by sequencing. The
753 list of strains and plasmids can be found in the Star Methods Key Resources Table.

754 **Fluorescence microscopy from batch cultures**

755 500 µl samples at indicated times during sporulation were taken and concentrated ~50-
756 fold by centrifugation (3300xg for 30 s). Membranes were stained with 1-(4-
757 trimethylammoniumphenyl)-6-phenyl-1,3,5-hexatriene *p*-toluenesulfonate (TMA-DPH;
758 Molecular Probes) at a final concentration of 100 µM and the cells were then
759 immobilized on a 2% agarose pad made with sporulation buffer covered with a no.1.5
760 coverslip, after which the cells were immediately imaged live. In most cases
761 fluorescence microscopy was performed using a Nikon Ti microscope equipped with a
762 ×100 Plan Apo 1.45 NA phase-contrast oil objective, an Orca-Flash4.0 V2 CMOS
763 camera (Hamamatsu Photonics, Shizuoka,Japan) and a Spectra X light engine
764 (Lumencor, Beaverton, OR, USA), all controlled by Nikon Elements software (Nikon
765 Corp. Tokyo, Japan). Excitation of TMA-DPH was achieved using the 395/25 nm band
766 of the SpectraX system and Chroma's ET 49000 single band filter set the DAPI filter set.
767 (λ_{ex}=395/25 nm; λ_{em}=431/28 nm). Excitation light intensity was set to 50% and exposure
768 times were 200 ms.

769 In experiments shown in Figure 6 and S3, cells were prepared following the same
770 procedure but visualized on a Leica DMi8 Wide-field Inverted Microscope equipped with
771 a HC PL APO 100× DIC objective (NA=1.40), and an Andor iXon Ultra 888 EMCCD
772 camera (Andor Technology Ltd., Belfast, Northern Ireland) and a Spectra X light engine
773 (Lumencor, OR,USA) controlled by the LAS X program (Leica Microsystems, Wetzlar,
774 Germany). Excitation of TMA-DPH was achieved using the 395/25 nm band of the
775 Spectra X system and the Leica DAPI filter set (λ_{ex}=395/25 nm; λ_{em}=460/50 nm).
776 Excitation light intensity was set to 50% and exposure times were 300 ms. .

777 Images were processed using the ImageJ software. Contours generated using
778 JFilament were coloured using Photoshop.

779

780 **Time-lapse fluorescence microscopy**

781 Cells were visualized on a Leica DMi8 Wide-field Inverted Microscope equipped with a
782 HC PL APO 100× DIC objective (NA=1.40) and an iXon Ultra 888 EMCCD Camera from
783 Andor Technology. Sporulation was induced at 37°C. To visualize the membranes,
784 0.5 µg/ml FM4-64 was added to the culture ∼1 hours after sporulation induction and
785 incubation continued for another hour. Then a 10 µl sample was taken and transferred
786 to an agarose pad prepared as described (Lopez-Garrido et al., 2018). Pictures were
787 taken in an environmental chamber at 37°C every 5 min for at least 2 hours. Excitation
788 of FM4-64 was achieved using the 575/25 nm band of the SpectraX system and a
789 custom FM4-64 filter set (λ_{ex}=395/25 nm; λ_{em}>610nm). Excitation light intensity was set
790 to 5% to minimize phototoxicity and exposure times were 100 ms. For presentation
791 purposes, sporangia were aligned vertically (with forespore on top) by rotating them
792 using ImageJ. Contours generated with JFilament were colored using Photoshop.

793

794 **Expression, purification, and labeling of recombinant proteins.**

795 FisB ECD and mutants were purified as described in (Landajuela et al., 2021). Briefly,
796 His_6-FisB ECD was expressed in *E. coli* BL21 (DE3) (New England Biolabs,
797 Ipswich,MA,USA) and purified using HisPur™ Ni-NTA Resin (Thermo-Fisher Scientific,
798 Waltham, MA, USA). Protein expression was induced with 1 mM IPTG at OD_{600} = 0.6
799 overnight at 16°C. Cells were harvested by centrifugation and the pellet was
800 resuspended in Lysis Buffer (20 mM HEPES, 500 mM NaCl, 0.5 mM TCEP, 20 mM
801 imidazole, 2% glycerol, 20 mM $MgCl_2$) and flash frozen in liquid nitrogen. Pellets were
802 thawed on ice and cells were lysed by 5 passes through a high-pressure homogenizer
803 (Avestin EmulsiFlex-C3, Ottawa, Canada). The lysate was spun down at 100,000 g and
804 the soluble fraction was incubated with HisPur™ Ni-NTA Resin for 2.5 h at 4°C while
805 rotating. The bound protein was washed sequentially with Lysis Buffer, Lysis Buffer
806 containing 50 mM and finally 100 mM Imidazole. The protein was eluted in Elution
807 Buffer (20 mM HEPES, 500 mM NaCl, 0.5 mM TCEP, 200 mM Imidazole, 2% glycerol,
808 20 mM MgCl2). The protein was concentrated using a Vivaspin® with a 10 kDa
809 molecular weight cutoff and the concentration determined by Bradford protein assay.
810 His6-FisB ECD G123C was labeled with iFluor555™ maleimide dye (AAT Bioquest,
811 Sunnyvale, CA, USA) by adding a 20x molar excess of dye to the protein and the
812 reaction was incubated overnight at 4°C. Free dye was removed using a HiPrep 20/10
813 (GE, Chicago, IL, USA) column.

814

815 **Giant Unilamellar Vesicle (GUV) preparation**

816 GUVs were formed by electroformation (Stockl et al., 2010). Briefly, chloroform-
817 dissolved lipids were mixed in a glass tube at desired ratios and spotted on two indium
818 tin oxide (ITO) coated glass slides. Organic solvent was removed by placing the lipid
819 films in a vacuum desiccator for at least 2 h. A short strip of copper conductive tape was
820 attached to each ITO slide which are then separated by a PTFE spacer and held
821 together with binder clips. The chamber was filled with 500 µl Swelling Buffer (SweBu, 1
822 mM HEPES, 0.25 M sucrose, 1 mM DTT) and sealed with Critoseal (McCormick
823 Scientific LLC, Saint Louis, MO, USA). GUVs were formed by applying a sinusoidal
824 voltage of 10 Hz and an amplitude of 1.8 V for at least 2 h at room temperature. GUV
825 membranes were labeled by including 1 mole % 1,2-dioleoyl-sn-glycero-3-
826 phosphoethanolamine-N-(7-nitro-2-1,3-benzoxadiazol-4-yl) (NBD-PE) or 1,1'-
827 dioctadecyl-3,3,3',3'-tetramethylindodicarbocyanine perchlorate (DiD) in the lipid
828 composition. In Figure 2, "100% PC" and "30% CL" membranes are composed of (all
829 mole %) 99% phosphatidylcholine (PC), 1% NBD-PE, and 30% *E. coli* cardiolipin (CL),
830 69% eggPC, 1% NBD-PE, respectively. Deflated GUVs were composed of (all mole %)
831 25% *E. coli* phosphatidylethanolamine (PE), 5% *E. coli* CL, 50% *E. coli*
832 phosphatidylglycerol (PG), 19% eggPC and 1% DiD or NBD-PE (BS mix). All lipids were
833 purchased from Avanti Polar Lipids (Alabaster, AL), except for DiD which was from
834 Thermo Fisher (Waltham, MA).

835 GUVs were imaged using a Nikon Eclipse TE2000-E microscope. Prior to adding the
836 GUVs, the imaging chamber was filled with a 5 mg/ml β-Casein (Sigma, Saint Louis, MI,
837 USA) solution to prevent attachment of the GUVs to the glass coverslip. The β-Casein

838 solution was removed and replaced with RB-EDTA.

839

840 **Fluorescence recovery after photobleaching (FRAP)**

841 *Protein mobility*. FRAP measurements were conducted using a Leica SP8 inverted
842 microscope in the same open imaging chamber. As described above, GUVs were
843 diluted in RB-EDTA (25 mM HEPES at pH 7.4, 850140 mM KCl, 1 mM EDTA, 0.2 mM
844 tris(2-carboxyethyl) phosphine) and incubated with 1 μM FisB ECD for 2-3h. A
845 rectangular area was chosen to bleach as indicated in Figure 2C. Five images (laser
846 power 0.7%) were recorded before bleaching, 10 during bleaching (laser power 100%)
847 and 60 after bleaching (laser power 0.7%).

848 The mean GUV intensity was determined using ImageJ. A segmented line (10 pixels
849 wide) was drawn to manually follow the GUV membrane. The line was smoothed using
850 'fit spine' and the mean pixel intensity was calculated. The background was determined
851 as the mean pixel value of a 20 x 20-pixel box (close to but outside the GUVs) and
852 subtracted from the mean pixel intensity of the GUVs.

853 *Lipid mobility.* To monitor lipid mobility in the presence or absence of FisB ECD, GUVs
854 (E.ColiPE :E.ColiCL:E.ColiPG:EggPC:Cy5-PC = 25:5:50:19:1) were prepared as
855 described above and deposited on top of a 0.1% poly-lysine treated glass-bottom dish.
856 After incubation for 30 min at room temperature, the poly-lysine solution was removed
857 and replaced with RB-EDTA. For some samples, 1 μM iFluor555-FisB ECD was added
858 and incubated with the GUVs for 1.5 h. Unbound FisB-ECD was washed with RB-EDTA
859 before imaging. Photobleaching was performed using a Leica SP8 inverted confocal
860 microscope by scanning the 633 nm and 649 nm beams operating at 100% laser power
861 over a rectangular region of interest (ROI, 2 μm by 2 μm). The focal plane was set to
862 mid-GUV height. Note that the bleached membrane area is the cross-section of the ROI
863 set in the imaging plane and the optical thickness (~1 μm), i.e. ~ 2 μm^2. Five frames
864 were acquired at low (1%) laser power for normalization of the fluorescence signal
865 before bleaching the ROI for 1.53 s and recovery was monitored for 60 frames every
866 154 ms at low laser power (1%). Image size was 128 x 128 pixels. The background was
867 determined with the same ROI area outside the vesicle using ImageJ and subtracted
868 from the signal. The mean pixel intensity of the entire GUV was used to correct for
869 photobleaching during low intensity excitation read-out after rescaling to account for
870 polarization effects. Because the unbleached lipid reservoir is finite, the mean pixel
871 intensity of the entire GUV decreases during the high-intensity bleach. The GUV
872 contour intensity just after bleaching was used as the maximum possible recovery value
873 when calculating the fractional recovery of the ROI fluorescence. To estimate fractional
874 recovery and an approximate recovery time, the corrected and averaged recovery
875 curves were fitted to $f(t) = f_\infty(1 - \exp(-t/\tau))$ where f_∞ and τ are the fractional
876 recovery and the recovery timescales, respectively.

877 **Image analysis**

878 **Determination of forespore and mother membrane surface area.** Using the ImageJ
879 plugin Filament 2D (Smith et al., 2010), "snakes" were fitted to forespores and mother
880 cells (Figure S1A). Snakes were fitted to forespores using either the TMA-DPH

881 membrane stain (using ridges) or a soluble CFP marker (using gradients) expressed in
882 the forespores. Snakes were fitted to mother cells using the corresponding phase
883 contrast image using gradients. In all cases the snakes were fitted as contours. Fitting
884 parameters were as follows: $\alpha = 100$, $\beta = 100$, $\gamma = 800$, weight=0.5, stretch force=100,
885 deform iterations=50, point spacing=0.5, image smoothing=1.01.

886 To determine the surface area of forespores and mother cells, the snakes were then
887 further analyzed with MATLAB. First, an ellipse was fitted to the snakes to determine
888 the symmetry axis of the forespore or mother cell (Figure S1B). Half of the snake is then
889 rotated around the symmetry axis to create a surface of revolution from which the
890 membrane surface area for the forespore or mother cell was determined (Figure S1C).

891 For the analyses shown in Figure 5I, FisB foci were semi-automatically selected using
892 SpeckleTrackerJ (Smith et al., 2011). For each spot, the sum of pixel values in a 6
893 pixels × 6 pixels (0.5 μm×0.5 μm) box around the center of the spot were calculated.
894 For each corresponding cell, the same operation was performed at a membrane area
895 where no clusters were present and subtracted from the individual FisB cluster intensity.

896 **Determination of mean fluorescence intensity around the forespore.** We used
897 ImageJ plugin Filament 2D to fit snakes around forespores (see above) to define
898 forespore contours. Mean contour intensity was calculated using Matlab, using snake
899 coordinates from Filament 2D dilated to 4 pixels used as a mask.

900

901 **Modeling.** Please see SI Appendix for details.

902

903 **SUPPLEMENTARY FIGURE LEGENDS**

904 **Figure S1. Forespore area changes can also be detected using a soluble marker.**
905 **Related to Figure 3. A.** Membrane fission was assessed by fluorescent microscopy
906 during a sporulation time course in wild type (BKM015) cells containing a fluorescent
907 forespore reporter (P_{spoIIQ}-*cfp*). Membranes were visualized with the fluorescent dye
908 TMA-DPH. Forespore contours in pre- and post-fission cells are indicated with blue or
909 red contours, respectively. Time (in hours) after the initiation of sporulation is indicated
910 as T2.5, T.3, etc.. Bar, 1 µm. **B.** Average post-fission forespore areas (A_{FS}) detected
911 using either marker grow while average pre-fission FS areas shrink as a function of time
912 into sporulation. Error bars represent SEM from three independent experiments (70
913 cells were analyzed per point).

914 **Figure S2. Blocking lipid synthesis inhibits forespore inflation and membrane**
915 **fission. Related to Figure 4. A.** Cerulenin (Cer) inhibits *de novo* synthesis of neutral
916 lipids and phospholipids by inhibiting *de novo* fatty acid biosynthesis. **B.** Representative
917 images showing cells at *t* = 3 h after addition of 10 µg/ml cerulenin at indicated
918 timepoints after nutrient downshift. Membranes were visualized with TMA-DPH. A cell
919 that is blocked at the asymmetric division stage is highlighted (red arrowhead). Scale
920 bars = 1 µm**. C.** Percentage of cells (wild-type strain, PY79) that have undergone
921 membrane fission at *t* = 3 h after addition of cerulenin at the indicated timepoints. More
922 than 300 cells were analyzed for each time point. **D**. Quantification of forespore
923 membrane area for cells that have (red) or have not (blue) undergone membrane fission
924 at *t* = 3 h after cerulenin addition at the indicated times after nutrient downshift (n=25-70
925 cells per data point). **E.** Fractional area occupied by the FS in pre- (blue) and post-
926 fission (red) cells at t = 3 h. Cerulenin was added at the indicated times after nutrient
927 downshift (n=25-70 cells per data point). **F**. Representative images showing cells (strain
928 BAM003) at t=3 hr after the nutrient downshift, with Cer application for the indicated
929 durations. Examples of cells with a discrete mGFP-FisB focus at the cell pole are
930 highlighted with green arrowheads. Scale bars represent 1 µm. **G.** Engulfment is
931 perturbed to a greater extent when lipid synthesis is inhibited earlier by cerulenin
932 addition (>300 cells per data point). **H**. Percentage of cells with FisB accumulation
933 (ISEP formation) at the membrane fission site, for cells that have visually completed
934 engulment. **I**. The fraction of post-fission cells among cells with correct FisB localization
935 (ISEP formation) as a function of increasing cerulenin application time (n=90-200 cells
936 were analyzed per point). Means±SEM of 3 independent experiments are shown for
937 panels C-E and G-I.

938 **Figure S3. Blocking forespore inflation inhibits membrane fission. Related to**
939 **Figure 4. A.** Engulfment and FisB localization in cells expressing wild-type (WT)
940 SpoIIIE or ATP-ase deficient SpoIIIE36. Membranes were labeled with TMA-DPH and
941 FisB was visualized using mGFP-FisB expressed at native levels on a *ΔfisB* background
942 (Landajuela et al., 2021). Fluorescence microscopy images were acquired 3 h after
943 nutrient downshift that initiated sporulation. Cells that have visually completed
944 engulfment and had accumulated FisB a the membrane fission site are indicated by
945 arrowheads. On the images on the right, detected FS contours are overlaid in blue and

946 red for pre- and post-fission cells. **B**. Percentage of cells that underwent membrane
947 fission as a function of time into sporulation, for WT and SpoIIIE36 cells. (For each data
948 point >300 cells were analyzed). **C**. FS areas as a function of time after nutrient
949 downshift, for pre- (blue) and post-fission (red) cells, expressing either WT (solid lines)
950 or ATPase deficient SpoIIIE (SpoIIIE36). (n=25-70 cells per data point) **D-F**. As in A-C,
951 but using cells expressing mGFP-FisB at ~8-fold lower levels (Landajuela et al., 2021).
952 **G**. FisB localization is affected when DNA translocation is completely blocked.
953 Percentage of cells displaying an intense spot at the engulfment pole (ISEP) for cells
954 expressing SpoIIIE^{WT} or SpoIIIE36 on a background with either native or reduced
955 mGFP-FisB levels. Scale bars = 1 μm. **H.** The fraction of post-fission cells among cells
956 with correct FisB localization (ISEP formation). (n=25-70 cells were analyzed per data
957 point). In panels B,C, E-H, mean±SEM of three independent biological replicates are
958 plotted for every point.

959 **Figure S4. Pre-fission forespores inflate in a low expression FisB strain in which**
960 **membrane fission is delayed. Related to Figure 5. A**. Summary of FisB copy number
961 quantification under native or low expression levels (Landajuela et al., 2021). Right.
962 Under native expression, on average, there are ~1,000 FisB molecules per cell at t=3 h.
963 Each DMC contains ~12 FisB molecules, while the ISEP contains ~40 FisB copies. In
964 the low-expression strain all the numbers are scaled down ~7-8-fold. **B.** Time course of
965 membrane fission for wild-type cells, *ΔfisB* cells, or *ΔfisB* cells complemented with
966 mGFP-FisB expressed at native (BAM003) or low levels (BAL003). (More than 300 cells
967 were analyzed per data point.) **C.** Fluorescence microscopy images of cells expressing
968 mGFP-FisB at the native level (BAM003) at 3 h into sporulation. Membranes were
969 visualized with TMA-DPH. Examples of a sporulating cell with a discrete mGFP-FisB
970 focus at the cell pole (intense spot at engulfment pole, ISEP) are highlighted with a red
971 arrowhead. In the panels on the right red contours indicate forespores that have
972 undergone fission whereas blue contours indicate forespores that have not yet
973 undergone membrane fission (70 cells per data point). Scale bars represent is 1 μm. **D.**
974 Similar to C but using a strain (BAL003) that expresses mGFP-FisB at lower levels in a
975 *ΔfisB* background. **E, F.** Under mGFP-FisB expression at low levels, both the average
976 pre- (E) and post-fission (F) forespore areas (A_{FS}) grow, in a manner qualitatively similar
977 to cells lacking FisB altogether (ΔFisB). By contrast, for cells expressing mGFP-FisB the
978 native level, the average pre- and post-fission FS areas decrease and increase as a
979 function of time into sporulation, respectively (70 cells were analyzed per data point).
980 Data for *ΔfisB* cells is copied from Figure 6 for comparison. In panels B, E, F,
981 mean±SEM of three independent replicates are plotted.

982 **Figure S5. Examples of forespore area growth and membrane fission detected at**
983 **the single cell level. Related to Figure 6.** Each top row of a triplet shows a unique cell
984 followed as a function of time in time-lapse fluorescence microscopy. Cell membranes
985 were labeled with FM4-64. Images are shown with an inverted look-up table. Frames
986 were acquired every 5 min. The middle and bottom rows of every triplet show the
987 overlaid contour of the FS or the MC membrane, respectively. The intensity of the FS

988 membrane starts decreasing upon membrane fission, because bleached FM4-64
989 molecules are confined and can no longer exchange with the unlabeled dyes in the bath
990 after membrane fission. For each cell, the mean FS contour intensity and the FS area
991 are shown on the right. The time of membrane fission (τ_{fiss}) estimated from the contour
992 intensity time profile is indicated on the FS area plots.

993

994

995

996 **REFERENCES**

997 Allemand, J.F., and Maier, B. (2009). Bacterial translocation motors investigated by single
998 molecule techniques. FEMS Microbiol Rev *33*, 593-610.

999 Bath, J., Wu, L.J., Errington, J., and Wang, J.C. (2000). Role of Bacillus subtilis SpoIIIE
1000 in DNA transport across the mother cell-prespore division septum. Science *290*, 995-997.

1001 Boron, W., and Boulpaep, E. (2017). Medical Physiology, 3 edn (Philadelphia, PA:
1002 Elsevier).

1003 Burton, B.M., Marquis, K.A., Sullivan, N.L., Rapoport, T.A., and Rudner, D.Z. (2007). The
1004 ATPase SpoIIIE transports DNA across fused septal membranes during sporulation in
1005 Bacillus subtilis. Cell *131*, 1301-1312.

1006 Campelo, F., and Malhotra, V. (2012). Membrane fission: the biogenesis of transport
1007 carriers. Annu Rev Biochem *81*, 407-427.

1008 Cochilla, A.J., Angleson, J.K., and Betz, W.J. (1999). Monitoring secretory membrane
1009 with FM1-43 fluorescence. Annu Rev Neurosci *22*, 1-10.

1010 Doan, T., Coleman, J., Marquis, K.A., Meeske, A.J., Burton, B.M., Karatekin, E., and
1011 Rudner, D.Z. (2013). FisB mediates membrane fission during sporulation in Bacillus
1012 subtilis. Genes Dev *27*, 322-334.

1013 Evans, E., Heinrich, V., Ludwig, F., and Rawicz, W. (2003). Dynamic tension
1014 spectroscopy and strength of biomembranes. Biophysical Journal *85*, 2342-2350.

1015 Ferguson, S.M., and De Camilli, P. (2012). Dynamin, a membrane-remodelling GTPase.
1016 Nat Rev Mol Cell Biol *13*, 75-88.

1017 Heath, R.J., and Rock, C.O. (2004). Fatty acid biosynthesis as a target for novel
1018 antibacterials. Curr Opin Investig Drugs *5*, 146-153.

1019 Karatekin, E., Sandre, O., Guitouni, H., Borghi, N., Puech, P.H., and Brochard-Wyart, F.
1020 (2003). Cascades of transient pores in giant vesicles: line tension and transport. Biophys
1021 J *84*, 1734-1749.

1022 Khanna, K., Lopez-Garrido, J., Zhao, Z., Watanabe, R., Yuan, Y., Sugie, J., Pogliano, K.,
1023 and Villa, E. (2019). The molecular architecture of engulfment during Bacillus subtilis
1024 sporulation. Elife *8*.

1025 Landajuela, A., Braun, M., Rodrigues, C.D.A., Martinez-Calvo, A., Doan, T., Horenkamp,
1026 F., Andronicos, A., Shteyn, V., Williams, N.D., Lin, C.X.*, et al.* (2021). FisB relies on homo-
1027 oligomerization and lipid binding to catalyze membrane fission in bacteria. Plos Biol *19*.

1028 Liu, N., Chistol, G., and Bustamante, C. (2015). Two-subunit DNA escort mechanism and
1029 inactive subunit bypass in an ultra-fast ring ATPase. Elife *4*.

1030 Liu, N., Chistol, G., Cui, Y., and Bustamante, C. (2018). Mechanochemical coupling and
1031 bi-phasic force-velocity dependence in the ultra-fast ring ATPase SpoIIIE. Elife *7*.

1032 Liu, N.J., Dutton, R.J., and Pogliano, K. (2006). Evidence that the SpoIIIE DNA
1033 translocase participates in membrane fusion during cytokinesis and engulfment. Mol
1034 Microbiol *59*, 1097-1113.

1035 Lopez-Garrido, J., Ojkic, N., Khanna, K., Wagner, F.R., Villa, E., Endres, R.G., and
1036 Pogliano, K. (2018). Chromosome Translocation Inflates Bacillus Forespores and
1037 Impacts Cellular Morphology. Cell *172*, 758-770 e714.

1038 Moir, A., and Cooper, G. (2015). Spore Germination. Microbiol Spectr *3*.

1039 Needham, D., and Nunn, R.S. (1990). Elastic-Deformation and Failure of Lipid Bilayer-
1040 Membranes Containing Cholesterol. Biophysical Journal *58*, 997-1009.

1041 Ojkic, N., Lopez-Garrido, J., Pogliano, K., and Endres, R.G. (2014). Bistable Forespore
1042 Engulfment in Bacillus subtilis by a Zipper Mechanism in Absence of the Cell Wall. Plos
1043 Comput Biol *10*, e1003912.

1044 Ojkic, N., López-Garrido, J., Pogliano, K., and Endres, R.G. (2016). Cell-wall remodeling
1045 drives engulfment during Bacillus subtilis sporulation. Elife *5*.

1046 Pedrido, M.E., de Ona, P., Ramirez, W., Lenini, C., Goni, A., and Grau, R. (2013). Spo0A
1047 links de novo fatty acid synthesis to sporulation and biofilm development in Bacillus
1048 subtilis. Mol Microbiol *87*, 348-367.

1049 Pogliano, K., Hofmeister, A.E., and Losick, R. (1997). Disappearance of the sigma E
1050 transcription factor from the forespore and the SpoIIE phosphatase from the mother cell
1051 contributes to establishment of cell-specific gene expression during sporulation in Bacillus
1052 subtilis. J Bacteriol *179*, 3331-3341.

1053 Renard, H.F., Johannes, L., and Morsomme, P. (2018). Increasing Diversity of Biological
1054 Membrane Fission Mechanisms. Trends Cell Biol *28*, 274-286.

1055 Schoneberg, J., Lee, I.H., Iwasa, J.H., and Hurley, J.H. (2017). Reverse-topology
1056 membrane scission by the ESCRT proteins. Nat Rev Mol Cell Biol *18*, 5-17.

1057 Schujman, G.E., Grau, R., Gramajo, H.C., Ornella, L., and de Mendoza, D. (1998). De
1058 novo fatty acid synthesis is required for establishment of cell type-specific gene
1059 transcription during sporulation in Bacillus subtilis. Mol Microbiol *29*, 1215-1224.

1060 Setlow, P. (2003). Spore germination. Current Opinion in Microbiology *6*, 550-556.

1061 Sharp, M.D., and Pogliano, K. (1999). An in vivo membrane fusion assay implicates
1062 SpoIIIE in the final stages of engulfment during Bacillus subtilis sporulation. Proc Natl
1063 Acad Sci U S A *96*, 14553-14558.

1064 Simunovic, M., Evergren, E., Callan-Jones, A., and Bassereau, P. (2019). Curving Cells
1065 Inside and Out: Roles of BAR Domain Proteins in Membrane Shaping and Its Cellular
1066 Implications. Annu Rev Cell Dev Biol *35*, 111-129.

1067 Simunovic, M., Manneville, J.B., Renard, H.F., Evergren, E., Raghunathan, K., Bhatia,
1068 D., Kenworthy, A.K., Voth, G.A., Prost, J., McMahon, H.T*., et al.* (2017). Friction Mediates
1069 Scission of Tubular Membranes Scaffolded by BAR Proteins. Cell *170*, 172-184 e111.

1070 Smith, M.B., Karatekin, E., Gohlke, A., Mizuno, H., Watanabe, N., and Vavylonis, D.
1071 (2011). Interactive, computer-assisted tracking of speckle trajectories in fluorescence
1072 microscopy: application to actin polymerization and membrane fusion. Biophys J *101*,
1073 1794-1804.

1074 Smith, M.B., Li, H., Shen, T., Huang, X., Yusuf, E., and Vavylonis, D. (2010).
1075 Segmentation and tracking of cytoskeletal filaments using open active contours.
1076 Cytoskeleton (Hoboken) *67*, 693-705.

1077 Sterlini, J.M., and Mandelstam, J. (1969). Commitment to Sporulation in Bacillus Subtilis
1078 and Its Relationship to Development of Actinomycin Resistance. Biochem J *113*, 29-+.

1079 Stockl, M., Nikolaus, J., and Herrmann, A. (2010). Visualization of lipid domain-specific
1080 protein sorting in giant unilamellar vesicles. Methods Mol Biol *606*, 115-126.

1081 Tiller, G.E., Mueller, T.J., Dockter, M.E., and Struve, W.G. (1984). Hydrogenation of triton
1082 X-100 eliminates its fluorescence and ultraviolet light absorption while preserving its
1083 detergent properties. Anal Biochem *141*, 262-266.

1084 Tocheva, E.I., Matson, E.G., Morris, D.M., Moussavi, F., Leadbetter, J.R., and Jensen,
1085 G.J. (2011). Peptidoglycan remodeling and conversion of an inner membrane into an
1086 outer membrane during sporulation. Cell *146*, 799-812.

1087 Vadia, S., Tse, J.L., Lucena, R., Yang, Z., Kellogg, D.R., Wang, J.D., and Levin, P.A.
1088 (2017). Fatty Acid Availability Sets Cell Envelope Capacity and Dictates Microbial Cell
1089 Size. Curr Biol *27*, 1757-1767 e1755.

1090 Webb, C.D., Teleman, A., Gordon, S., Straight, A., Belmont, A., Lin, D.C., Grossman,
1091 A.D., Wright, A., and Losick, R. (1997). Bipolar localization of the replication origin regions
1092 of chromosomes in vegetative and sporulating cells of B. subtilis. Cell *88*, 667-674.

1093 Wu, L.J., and Errington, J. (1994). Bacillus subtilis SpoIIIE protein required for DNA
1094 segregation during asymmetric cell division. Science *264*, 572-575.

1095 Wu, L.J., and Errington, J. (1997). Septal localization of the SpoIIIE chromosome
1096 partitioning protein in Bacillus subtilis. EMBO J *16*, 2161-2169.

1097 Wu, L.J., and Errington, J. (1998). Use of asymmetric cell division and spoIIIE mutants to
1098 probe chromosome orientation and organization in Bacillus subtilis. Mol Microbiol *27*, 777-
1099 786.

1100 Yao, Z., Davis, R.M., Kishony, R., Kahne, D., and Ruiz, N. (2012). Regulation of cell size
1101 in response to nutrient availability by fatty acid biosynthesis in *Escherichia coli*.
1102 Proceedings of the National Academy of Sciences *109*, E2561.

1103 Youngman, P.J., Perkins, J.B., and Losick, R. (1983). Genetic transposition and
1104 insertional mutagenesis in Bacillus subtilis with Streptococcus faecalis transposon Tn917.
1105 Proc Natl Acad Sci U S A *80*, 2305-2309.

1106 Zhang, Y.M., and Rock, C.O. (2008). Membrane lipid homeostasis in bacteria. Nat Rev
1107 Microbiol *6*, 222-233.

1108

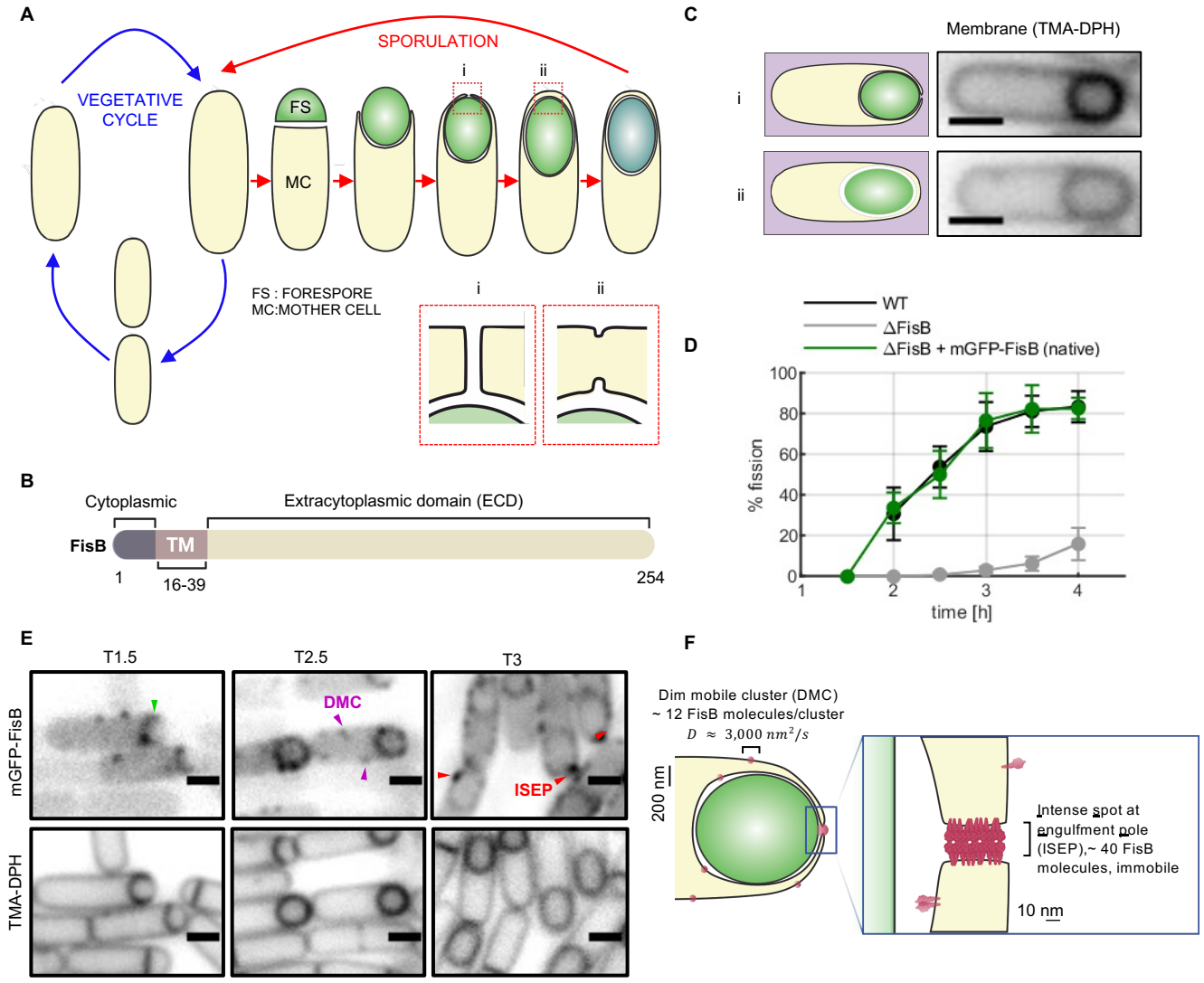
A
SPORULATION
VEGETATIVE CYCLE
FS
MC
i
ii
FS : FORESPORE
MC:MOTHER CELL
B
Cytoplasmic
Extracytoplasmic domain (ECD)
FisB
TM
1
16-39
254
C
Membrane (TMA-DPH)
D
WT
ΔFisB
ΔFisB + mGFP-FisB (native)
% fission
time [h]
E
T1.5
T2.5
T3
mGFP-FisB
TMA-DPH
DMC
ISEP
F
Dim mobile cluster (DMC)
~ 12 FisB molecules/cluster
$D \approx 3{,}000\ nm^2/s$
200 nm
Intense spot at engulfment pole (ISEP),~ 40 FisB molecules, immobile
10 nm

FIGURE 1

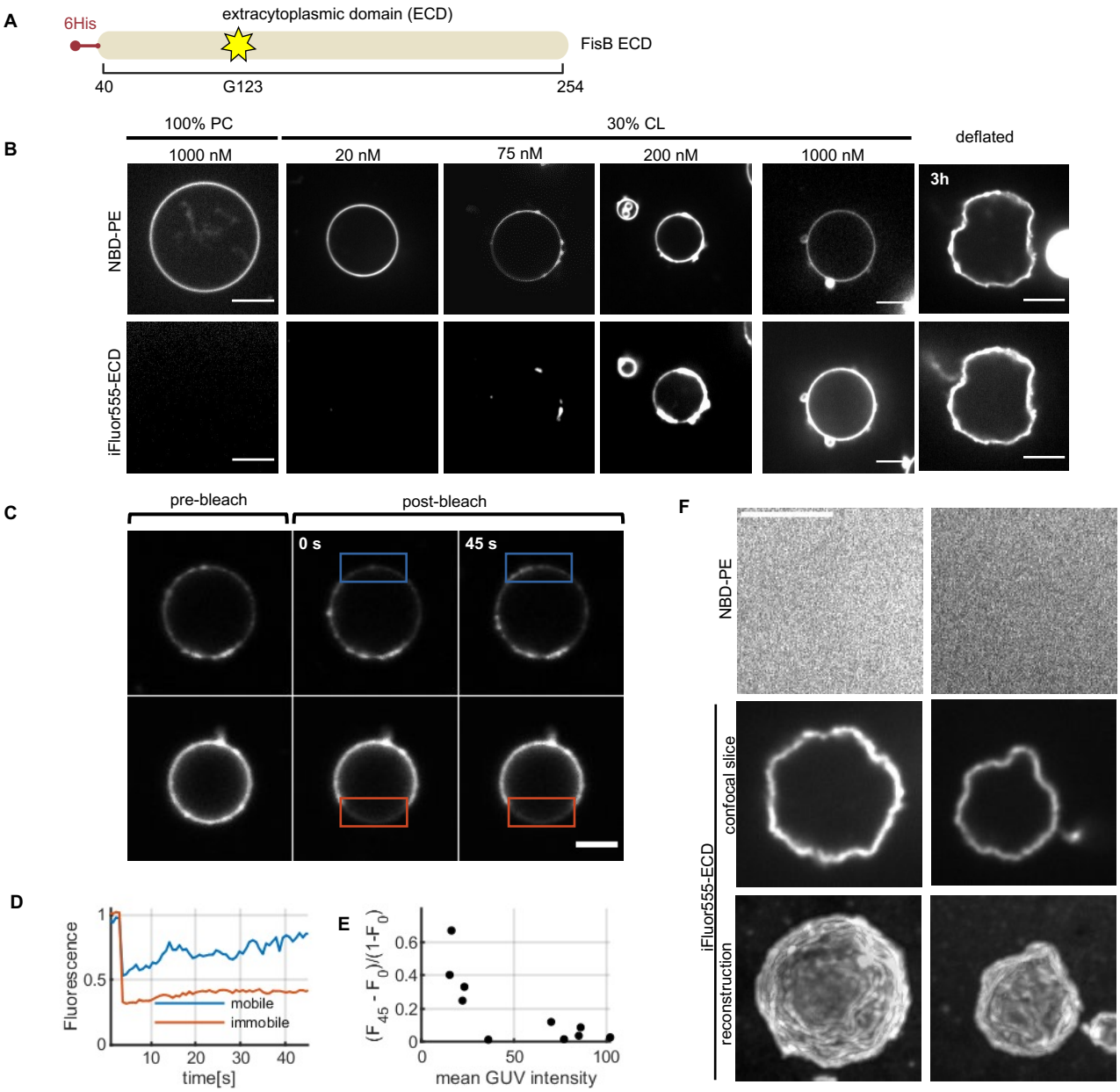
A
6His
extracytoplasmic domain (ECD)
FisB ECD
40
G123
254
B
100% PC
30% CL
deflated
1000 nM
20 nM
75 nM
200 nM
1000 nM
3h
NBD-PE
iFluor555-ECD
C
pre-bleach
post-bleach
0 s
45 s
D
Fluorescence
time[s]
mobile
immobile
E
(F45 - F0)/(1-F0)
mean GUV intensity
F
NBD-PE
iFluor555-ECD
confocal slice
reconstruction

FIGURE 2

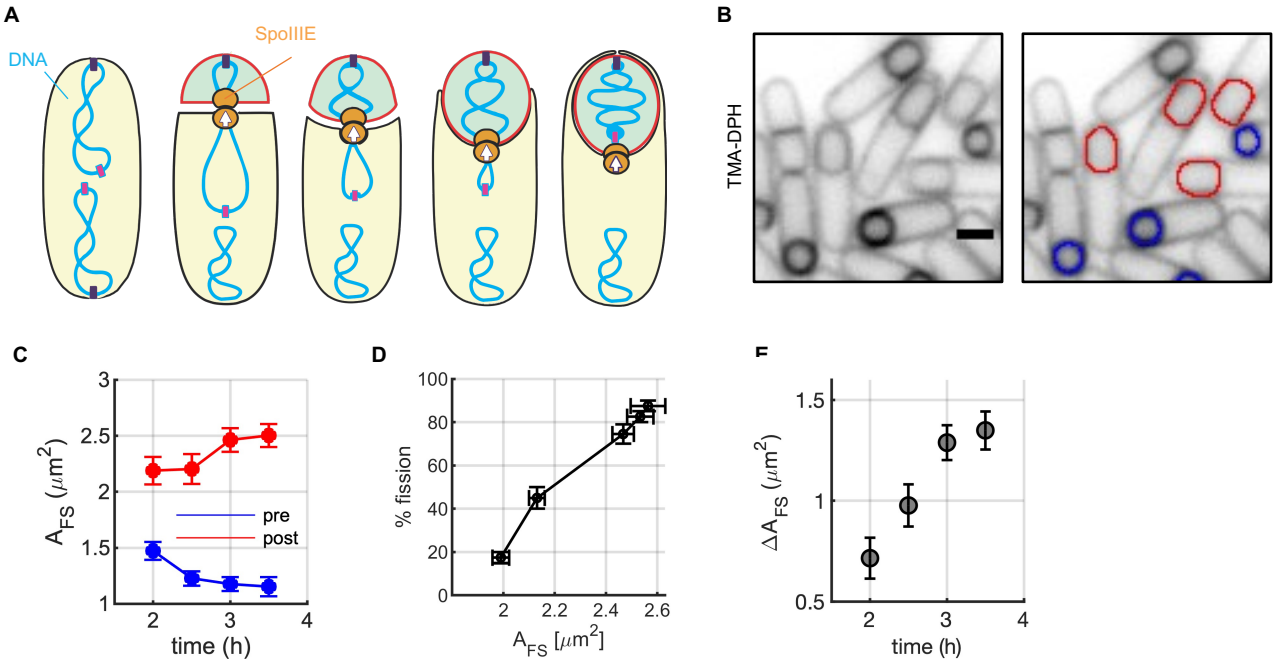
A
DNA
SpoIIIE
B
TMA-DPH
C
A_{FS} (μm^2)
time (h)
pre
post
D
% fission
A_{FS} [μm^2]
E
ΔA_{FS} (μm^2)
time (h)

FIGURE 3

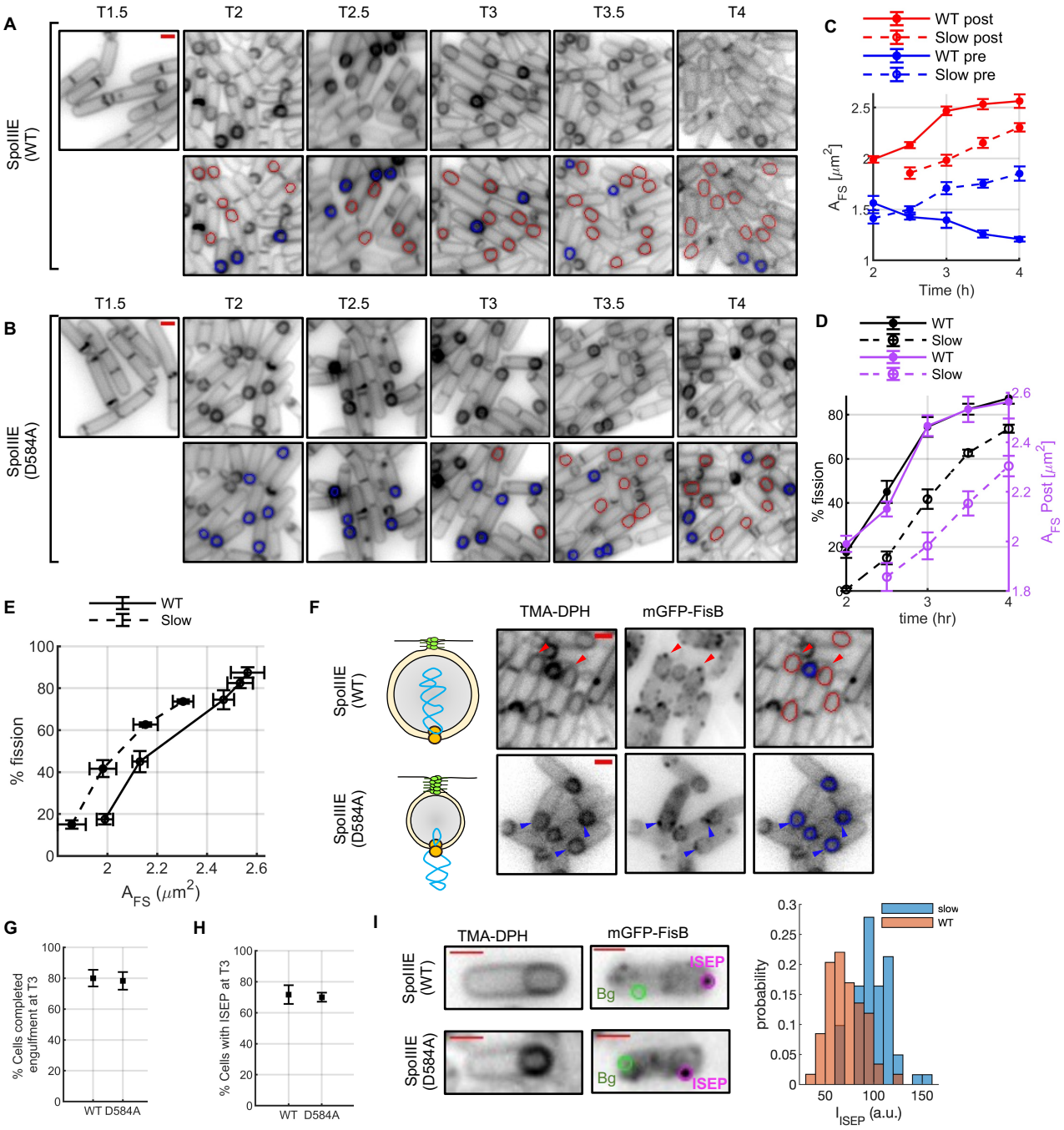
A
T1.5
T2
T2.5
T3
T3.5
T4
SpoIIIE (WT)
B
SpoIIIE (D584A)
C
WT post
Slow post
WT pre
Slow pre
A_{FS} [μm^2]
Time (h)
D
WT
Slow
WT
Slow
% fission
A_{FS} Post [μm^2]
time (hr)
E
WT
Slow
% fission
A_{FS} (μm^2)
F
TMA-DPH
mGFP-FisB
SpoIIIE (WT)
SpoIIIE (D584A)
G
% Cells completed engulfment at T3
WT D584A
H
% Cells with ISEP at T3
WT D584A
I
TMA-DPH
mGFP-FisB
SpoIIIE (WT)
SpoIIIE (D584A)
ISEP
Bg
slow
WT
probability
I_{ISEP} (a.u.)

FIGURE 4

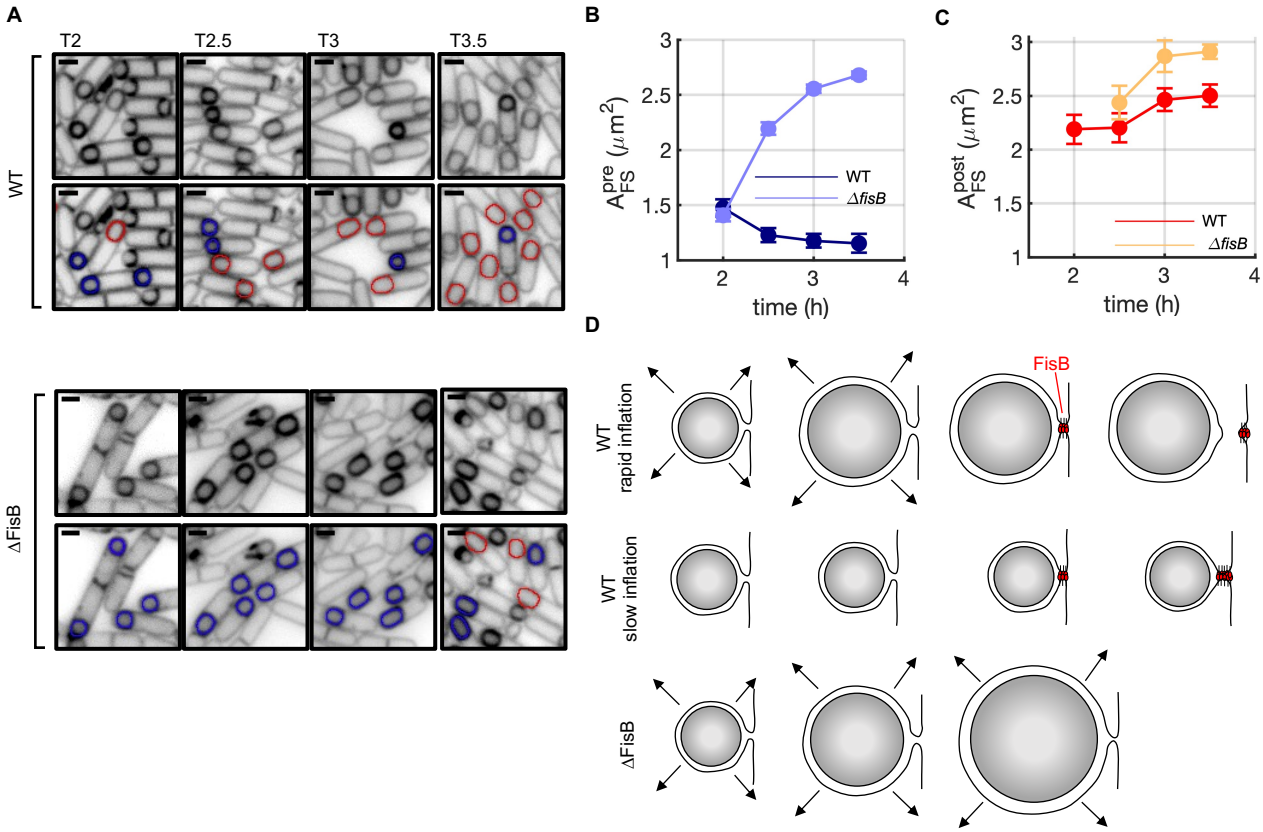
A
T2
T2.5
T3
T3.5
WT
ΔFisB
B
A_{FS}^{pre} (μm^2)
time (h)
WT
ΔfisB
C
A_{FS}^{post} (μm^2)
time (h)
WT
ΔfisB
D
WT rapid inflation
FisB
WT slow inflation
ΔFisB

FIGURE 5

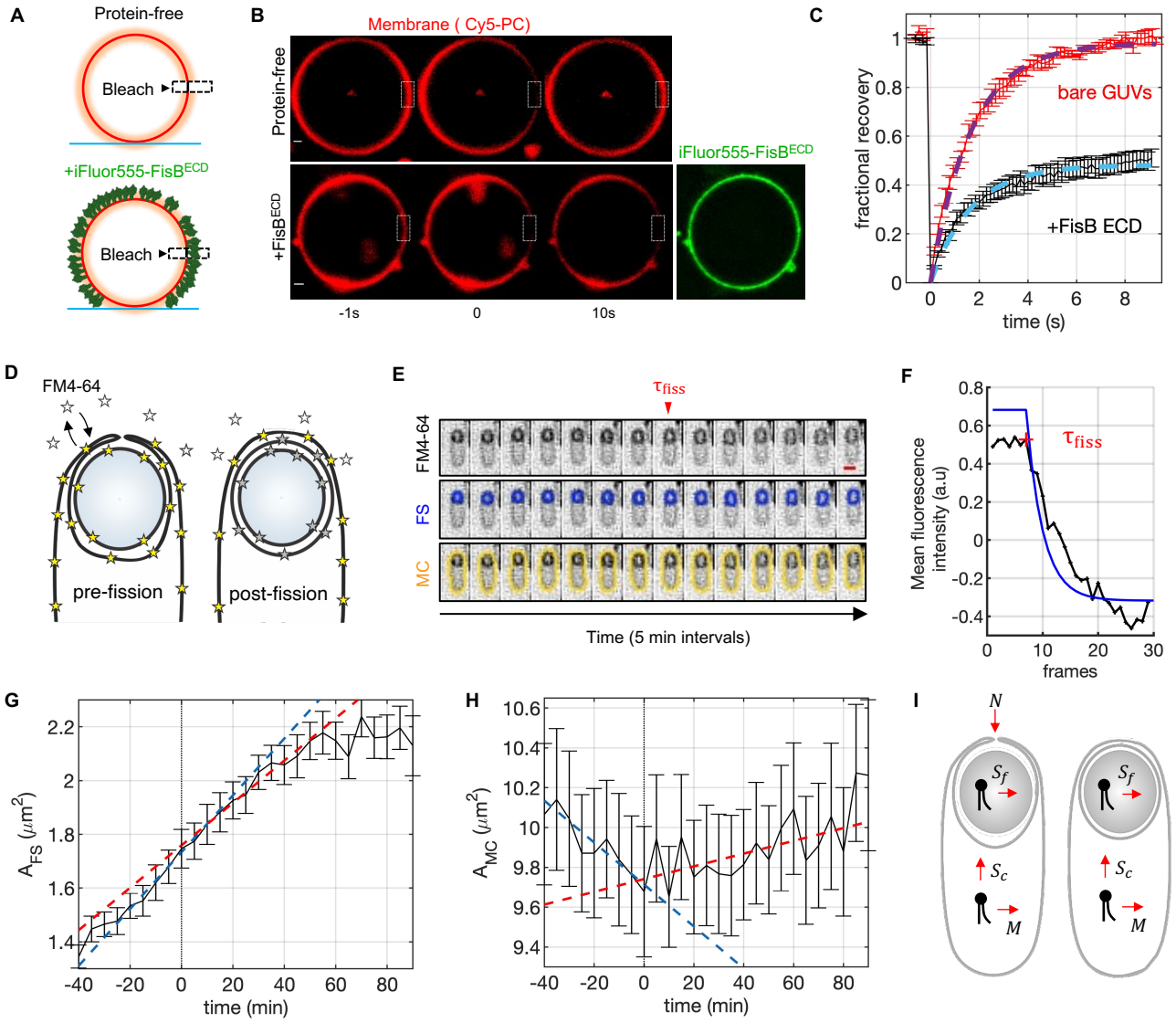
A
Protein-free
Bleach
+iFluor555-FisB^{ECD}
Bleach
B
Membrane (Cy5-PC)
Protein-free
+FisB^{ECD}
iFluor555-FisB^{ECD}
-1s
0
10s
C
fractional recovery
bare GUVs
+FisB ECD
time (s)
D
FM4-64
pre-fission
post-fission
E
τ_{fiss}
FM4-64
FS
MC
Time (5 min intervals)
F
τ_{fiss}
Mean fluorescence intensity (a.u)
frames
G
A_{FS} (μm^2)
time (min)
H
A_{MC} (μm^2)
time (min)
I
N
S_f
S_c
M

FIGURE 6

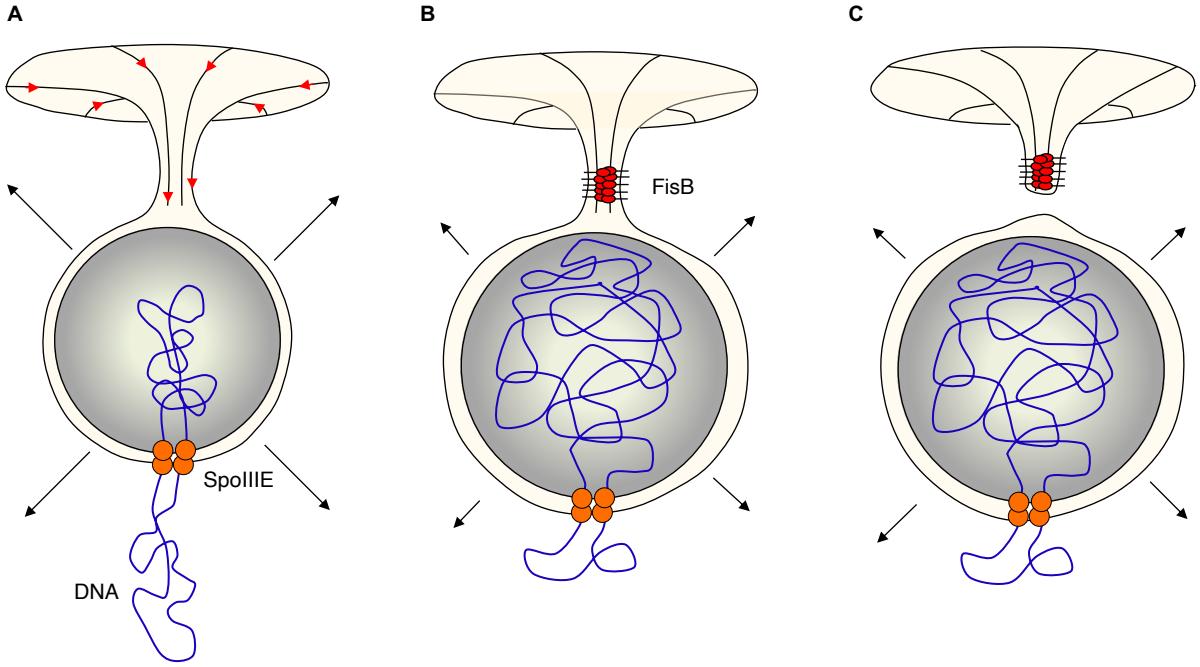

FIGURE 7

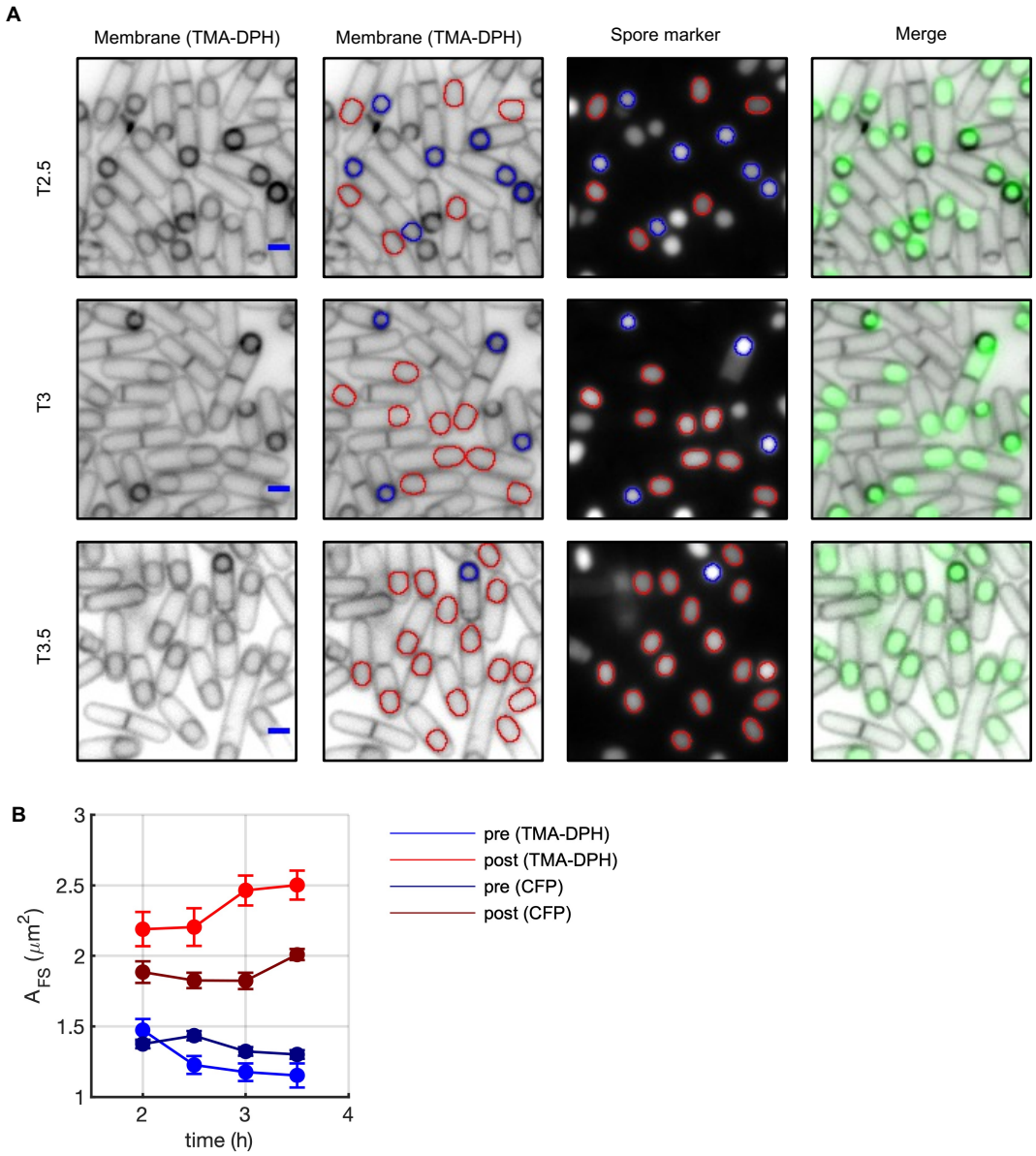
A
Membrane (TMA-DPH)
Membrane (TMA-DPH)
Spore marker
Merge
T2.5
T3
T3.5
B
pre (TMA-DPH)
post (TMA-DPH)
pre (CFP)
post (CFP)
A_{FS} (μm^2)
time (h)
1
1.5
2
2.5
3
2
3
4

FIGURE S1

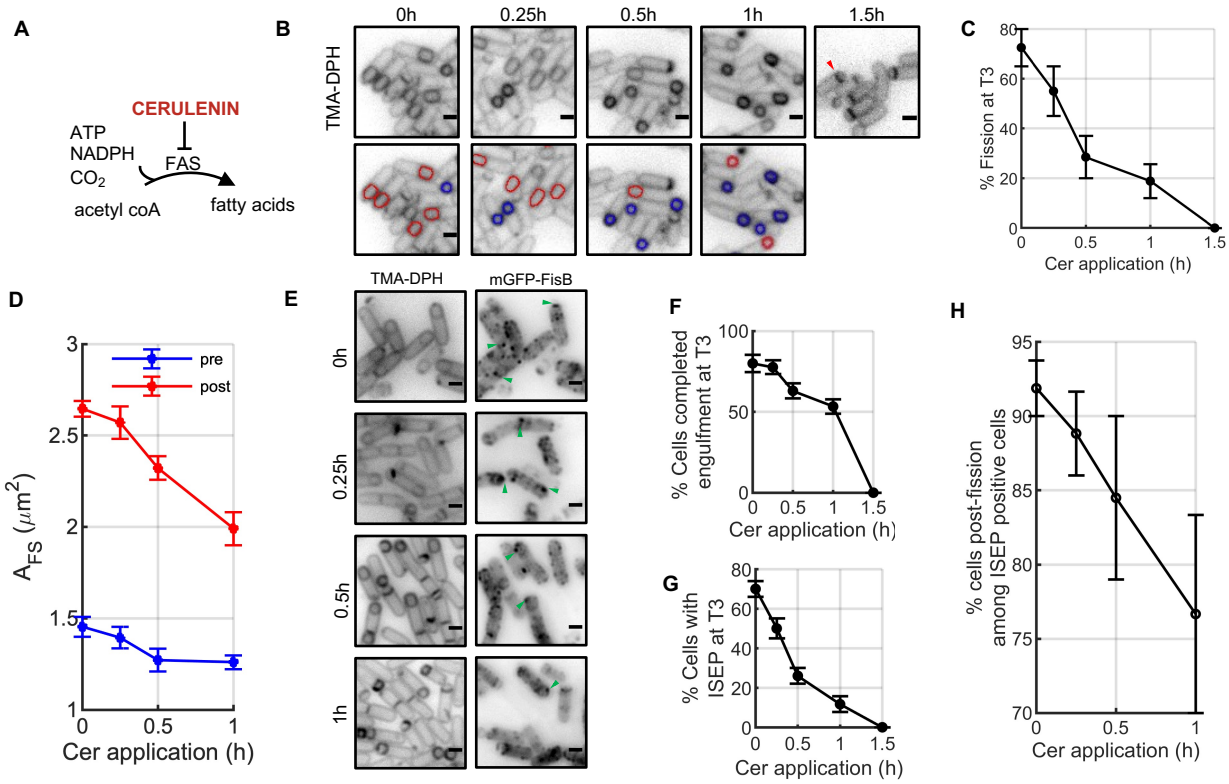
A
CERULENIN
ATP
NADPH
CO_2
FAS
acetyl coA
fatty acids
B
0h
0.25h
0.5h
1h
1.5h
TMA-DPH
C
% Fission at T3
Cer application (h)
D
pre
post
A_{FS} (μm^2)
Cer application (h)
E
TMA-DPH
mGFP-FisB
0h
0.25h
0.5h
1h
F
% Cells completed engulfment at T3
Cer application (h)
G
% Cells with ISEP at T3
Cer application (h)
H
% cells post-fission among ISEP positive cells
Cer application (h)

FIGURE S2

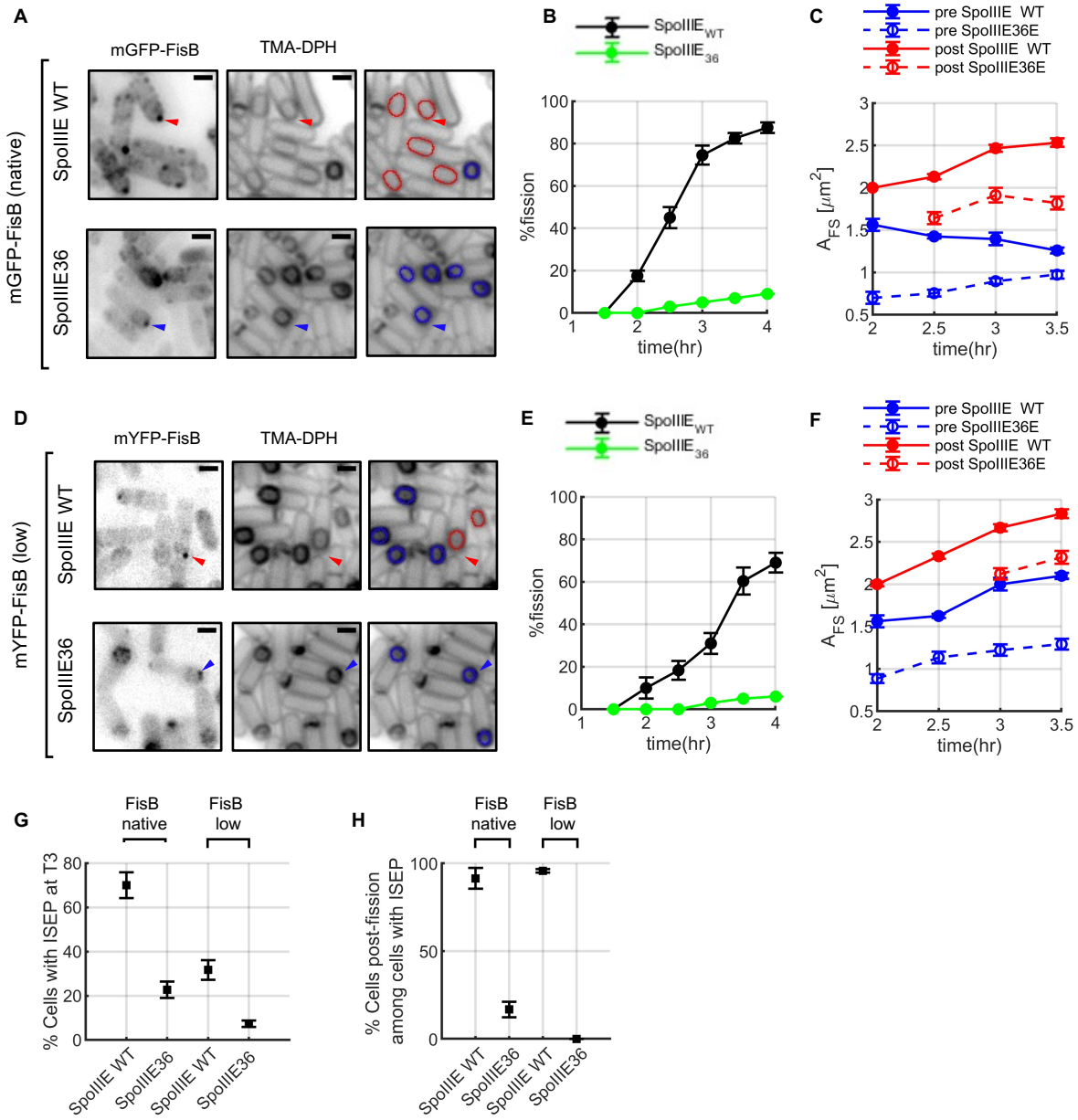
A
mGFP-FisB
TMA-DPH
mGFP-FisB (native)
SpoIIIE WT
SpoIIIE36
B
SpoIIIE$_{WT}$
SpoIIIE$_{36}$
%fission
time(hr)
C
pre SpoIIIE WT
pre SpoIIIE36E
post SpoIIIE WT
post SpoIIIE36E
A_{FS} [μm^2]
time(hr)
D
mYFP-FisB
TMA-DPH
mYFP-FisB (low)
SpoIIIE WT
SpoIIIE36
E
SpoIIIE$_{WT}$
SpoIIIE$_{36}$
%fission
time(hr)
F
pre SpoIIIE WT
pre SpoIIIE36E
post SpoIIIE WT
post SpoIIIE36E
A_{FS} [μm^2]
time(hr)
G
FisB native
FisB low
% Cells with ISEP at T3
SpoIIIE WT
SpoIIIE36
SpoIIIE WT
SpoIIIE36
H
FisB native
FisB low
% Cells post-fission among cells with ISEP
SpoIIIE WT
SpoIIIE36
SpoIIIE WT
SpoIIIE36

FIGURE S3

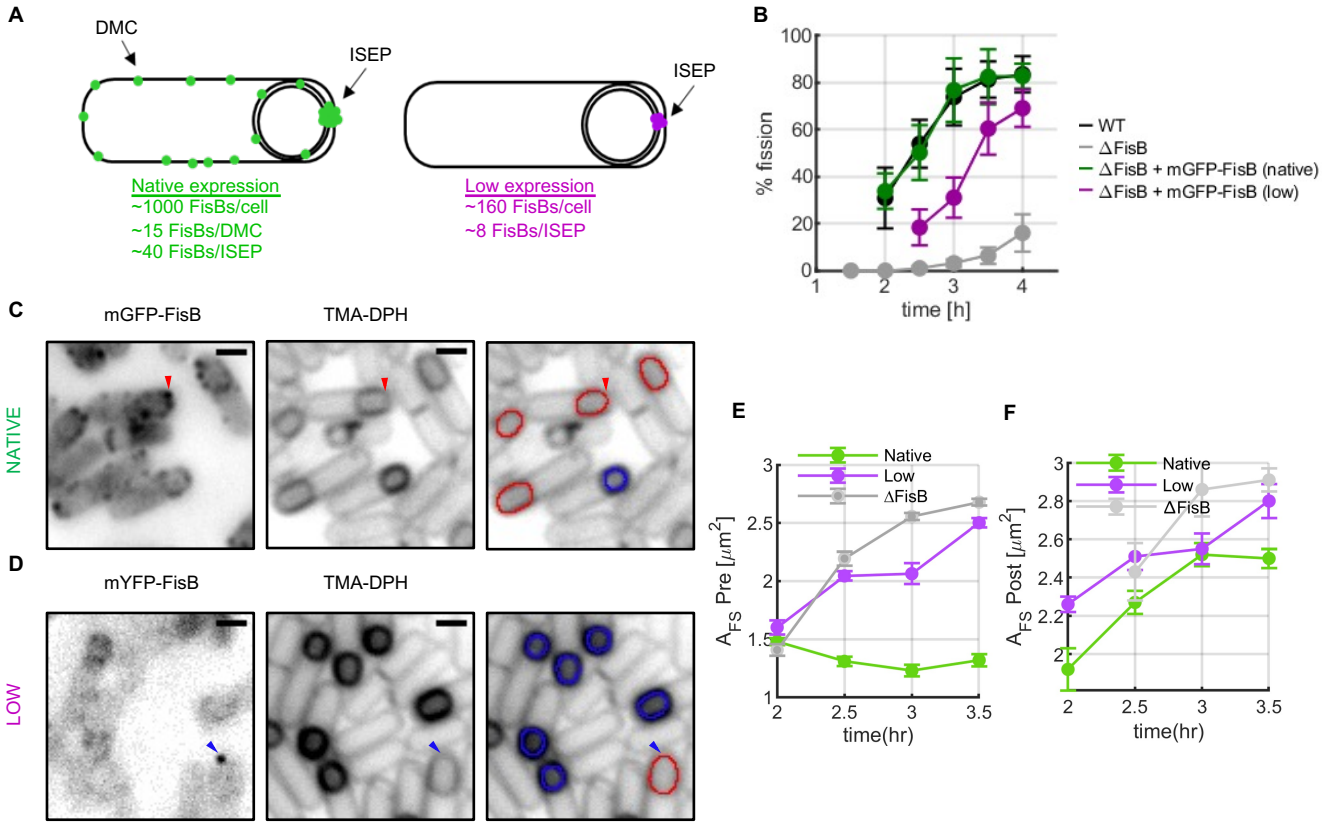
A
DMC
ISEP
ISEP
Native expression
~1000 FisBs/cell
~15 FisBs/DMC
~40 FisBs/ISEP
Low expression
~160 FisBs/cell
~8 FisBs/ISEP
B
% fission
time [h]
WT
ΔFisB
ΔFisB + mGFP-FisB (native)
ΔFisB + mGFP-FisB (low)
C
mGFP-FisB
TMA-DPH
NATIVE
D
mYFP-FisB
TMA-DPH
LOW
E
Native
Low
ΔFisB
A_{FS} Pre [μm^2]
time(hr)
F
Native
Low
ΔFisB
A_{FS} Post [μm^2]
time(hr)

FIGURE S4

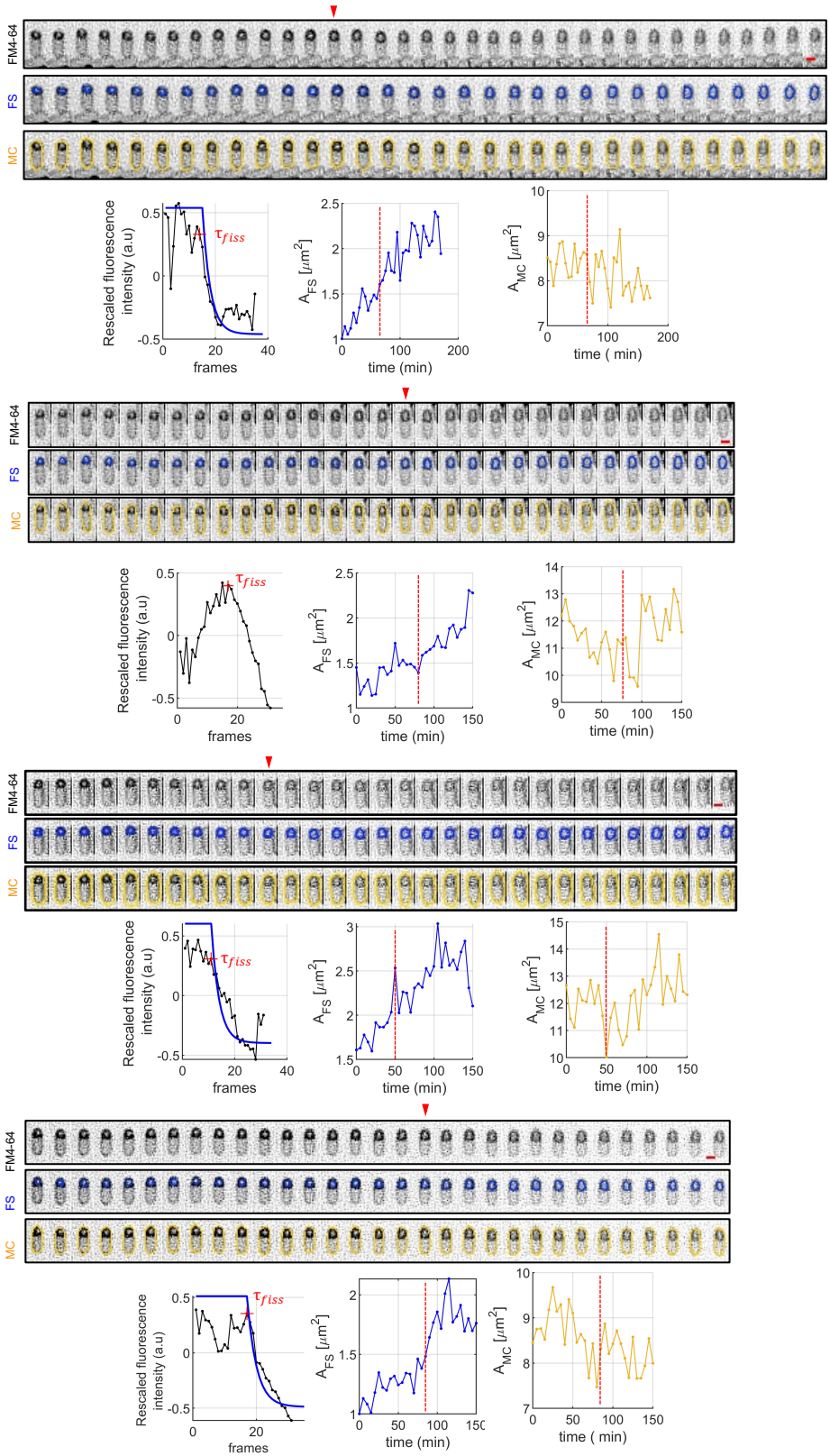
FM4-64
FS
MC
Rescaled fluorescence intensity (a.u)
τ_{fiss}
frames
A_{FS} [μm^2]
time (min)
A_{MC} [μm^2]
time (min)

FIGURE S5

SI Appendix: Theoretical Modeling

In previous work [1] we showed that a neck of radius $\leq 5-10$ nm in the region where the engulfment membrane meets the rest of the mother cell membrane (see sketch in Fig. 1a) is necessary for FisB to accumulate. This accumulation in turn favors membrane fission, as shown in the current main text. In this appendix, first, we develop a minimal model for the neck based on free-energy minimization. This minimal model assumes a highly simplified geometry of the membrane neck, as depicted in Fig. 1(b), that accounts for membrane tension, bending, and an osmotic pressure difference, $\Delta\tilde{p} = p_{\text{cyto}} - p_{\text{peri}}$, between the cytoplasm and periplasm since the lumen of the neck is continuous with the periplasmic space. Using this model, we explore if an increase of membrane tension in the neck, e.g. due to forespore inflation, along with the osmotic pressure difference are able to narrow the radius of the neck. Then, we consider a more realistic model by solving the complete Helfrich equation [2] including the possibility of a pulling force on the neck, e.g. due to DNA translocation through the SpoIIIE motor. For this more realistic model, the shape of the membrane neck is obtained as part of the solution.

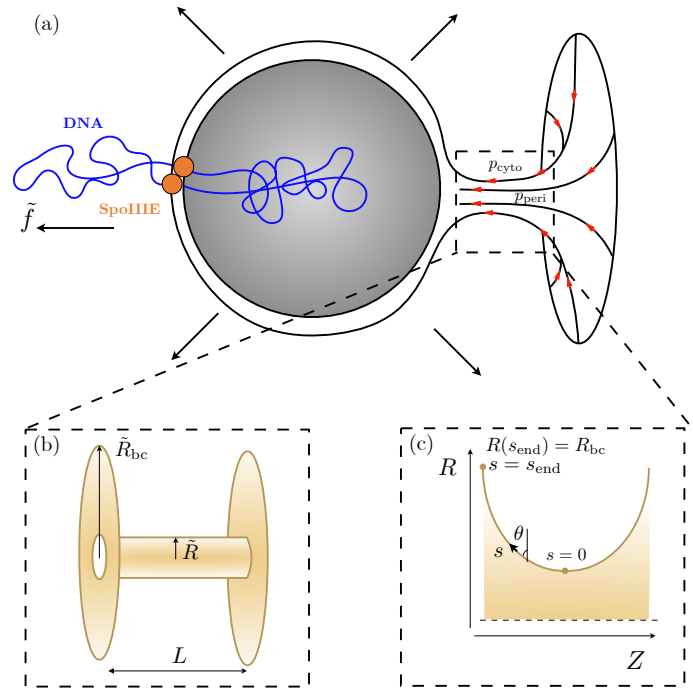

Figure 1. (a) Sketch of the engulfment membrane geometry during the last stage of forespore engulfment, showing the flow of lipids through the membrane neck, the osmotic pressure difference $\Delta\tilde{p} = p_{\text{cyto}} - p_{\text{peri}}$ between the cytoplasm and the periplasm, and the pulling force $\tilde{f}$ due to the SpoIIIE motors translocating DNA into the forespore. (b) Simplified model of the membrane neck, consisting of a straight cylinder of radius $\tilde{R}$ and length L, connecting two planar membranes of radius $\tilde{R}_{\text{bc}}$. (c) Schematic of the more realistic model of the membrane neck showing the parametrization of the surface, where s is the arc length along the contour and θ the angle with respect to the vertical.

MINIMAL MODEL FOR THE NECK: UNIFORM CYLINDER CONNECTING TWO PLANAR MEMBRANES

We first consider a highly simplified model based on the free energy $\tilde{\mathscr{F}}_0$ of an axisymmetric cylindrical membrane neck of radius $\tilde{R}$ and length L that connects two planar membrane sheets, corresponding to the local geometry depicted in 1(b). We employ the classical Helfrich-Canham theory [2–7] for the energy of the membrane, $\tilde{\mathscr{F}}_0$, which reads

$$\tilde{\mathscr{F}}_0 = \int_{S_{\text{n}}} \mathrm{d}S_{\text{n}} \left[\frac{\kappa}{2}(2\tilde{H})^2 + \gamma\right] + \int_{S_{\text{s}}} \mathrm{d}S_{\text{s}}\gamma + \int_{\tilde{V}} \mathrm{d}\tilde{V}\Delta\tilde{p}, \qquad (1)$$

where S_{n} and S_{s} are the surfaces of the membrane neck and sheets, and $\tilde{V}$ is the volume inside the neck. The tildes denote dimensional variables which will subsequently be non-dimensionalized. Here $\tilde{H}$ is the mean curvature, κ is the bending modulus, γ is the membrane surface tension, and $\Delta\tilde{p} = p_{\text{cyto}} - p_{\text{peri}}$ is the osmotic pressure difference. The two surrounding membrane sheets are assumed to be planar since their curvature is much less than that of the neck, thus their only contribution to the energy comes from their area times the membrane tension. In this simplified model, we neglect the bending energy of the junctions where the cylinder meets the membrane sheets. With these simplifications, the free energy $\mathscr{F}_0$ in Eq. (1) reads:

$$\frac{\tilde{\mathscr{F}}_0}{2\pi} = \left(\gamma\tilde{R} + \frac{\kappa}{2\tilde{R}}\right)L + \gamma(\tilde{R}_{\text{bc}}^2 - \tilde{R}^2) + \frac{\Delta\tilde{p}}{2}\tilde{R}^2 L, \qquad (2)$$

where $\tilde{R}_{\text{bc}} > \tilde{R}$ is the outer boundary condition depicted in Fig. 1(b). Minimizing Eq. (2) with respect to the radius $\tilde{R}$ yields

$$2\gamma\tilde{R}^2 - \kappa + 2\tilde{R}^3\left(\Delta\tilde{p} - \frac{2\gamma}{L}\right) = 0. \qquad (3)$$

To non-dimensionalize Eqs. (2)–(3) we introduce the natural length scale arising from the balance between bending and tension in Eq. (1) [8] as the characteristic length scale, $R_{\text{c}} = \sqrt{\kappa/(2\gamma)}$, and define $R = \tilde{R}/R_{\text{c}}$. The free energy is also made dimensionless as $\mathscr{F}_0 = \tilde{\mathscr{F}}_0/(\gamma R_{\text{c}} L)$. Hence, the dimensionless forms of Eqs. (2) and (3) read:

$$\frac{\mathscr{F}_0}{2\pi} = R + \frac{1}{R} + \frac{(R_{\text{bc}}^2 - R^2)}{L/R_{\text{c}}} + \frac{\Delta p}{2}R^2, \qquad (4)$$

$$R^2 - 1 + R^3\left(\Delta p - \frac{2}{L/R_{\text{c}}}\right) = 0, \qquad (5)$$

where $\Delta p = \Delta\tilde{p}R_{\text{c}}/\gamma$.

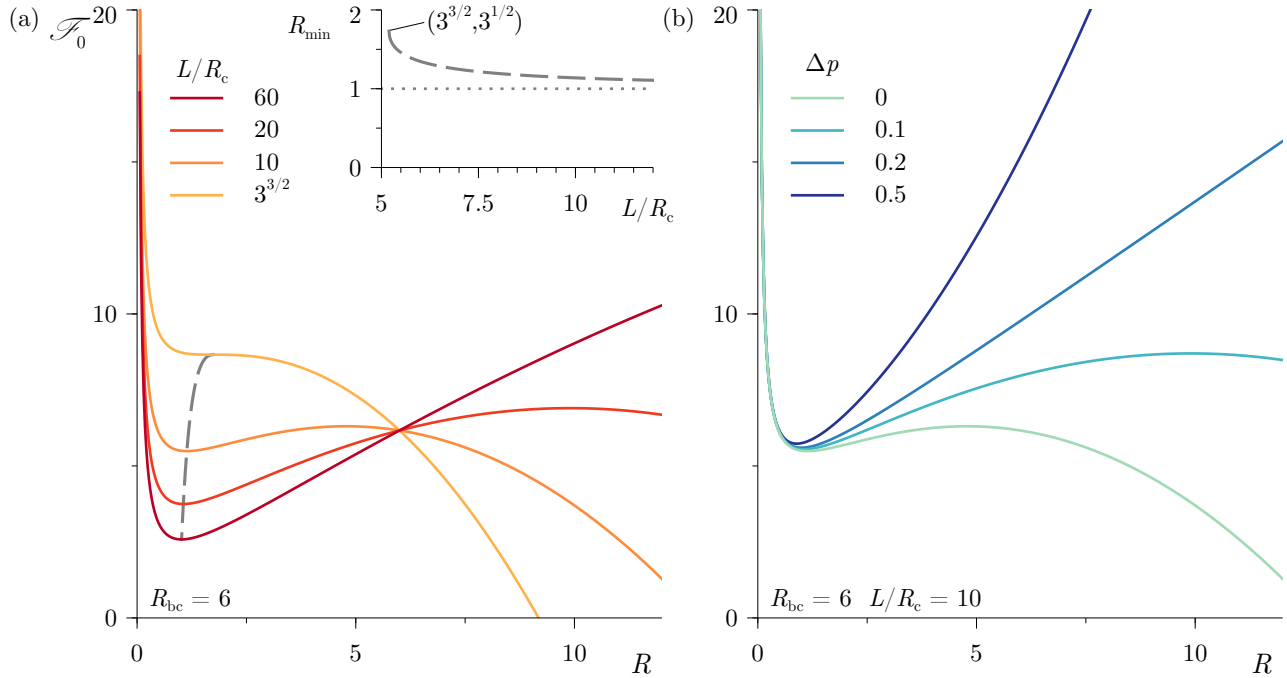

Figure 2. (a) Dimensionless free energy $\mathscr{F}_0 = \tilde{\mathscr{F}}_0/(\gamma R_c L)$ from Eq. (4) as a function of the dimensionless neck radius R, highlighting the existence of a local free-energy minimum provided $L/R_c > 3^{3/2}$ (gray dashed curve). Here $R_{bc} = 6$ and $\Delta p = 0$. The inset shows the corresponding radius R_{min} of the local free-energy minimum as a function of L/R_c. (b) Same as in panel (a) but for different values of the dimensionless osmotic pressure difference Δp, for a fixed length of the neck, $L/R_c = 10$.

Zero osmotic pressure difference. The solution of Eqs. (4) and (5) when $\Delta p = 0$ reveals that for a long enough neck there is a metastable state of the neck at finite radius R_{min} [9, 10]. This local minimum arises from a balance between membrane bending energy, which always favors larger R, and membrane tension, which contributes a non-monotonic function of R to the membrane energy. The existence of this local minimum can be observed in Fig. 2, which shows the dimensionless free energy $\mathscr{F}_0$ as a function of R for different values of L/R_c, along with the location R_{min} of the local minimum. Intuitively, for R around R_{min}, increasing the radius R increases the total amount of membrane in the vicinity of the neck and so increasing R is opposed by surface tension. By contrast, for larger values of R, increasing R removes more membrane from the parallel sheets (removed area scaling $\sim R^2$) than is added to the neck (added area scaling $\sim LR$), so further increase of R is energetically favored (specifically when $R > \sqrt{3} + \sqrt{2}\sqrt{L/R_c - 3\sqrt{3}}/3^{3/4} + O(L/R_c)$). We find that, for lengths below a critical value $L/R_c < 3^{3/2}$, the energy functional $\mathscr{F}_0$ does not have a local minimum, so that expanding the radius of the neck always decreases the total energy of the system, implying the neck opens.

Finite osmotic pressure difference. Eq. (5) indicates that a positive osmotic pressure difference between the cytoplasm and the periplasm favors the formation of a locally stable, narrow membrane neck. Indeed, the critical neck length below which there is no locally stable narrow neck decreases as Δp increases, $L/R_c \leq 2 \cdot 3^{3/2}/(2 + 3^{3/2}\Delta p)$. Moreover, the local maxima shown in Fig. 2(a) for $\Delta p = 0$, disappears when $\Delta p > 2/(L/R_c)$, as shown in Fig. 2(b). This implies that the free energy $\mathscr{F}_0$ increases monotonically beyond the local minimum, i.e. the neck will not open up. Moreover, the minimum radius of the neck R_{min} always decreases as Δp increases.

EQUILIBRIUM SHAPES OF THE AXISYMMETRIC MEMBRANE NECK

We now go beyond the minimal model described in the previous section by solving the complete Helfrich equation, where the shape of the neck is obtained as part of the solution. To this end, we describe the equilibrium shape of an axisymmetric and mirror symmetric membrane neck connecting two membrane sheets, corresponding to the local geometry of the neck connecting the forespore engulfing and mother cell membranes (see Figs. 1a and c). The energy functional $\tilde{\mathscr{F}}$ consists of a term accounting for membrane bending and tension, $\tilde{\mathscr{F}}_m$, another term accounting for the osmotic pressure pressure difference between cytoplasm and periplasm, $\tilde{\mathscr{F}}_p$, and a term representing any pulling force f on the forespore,

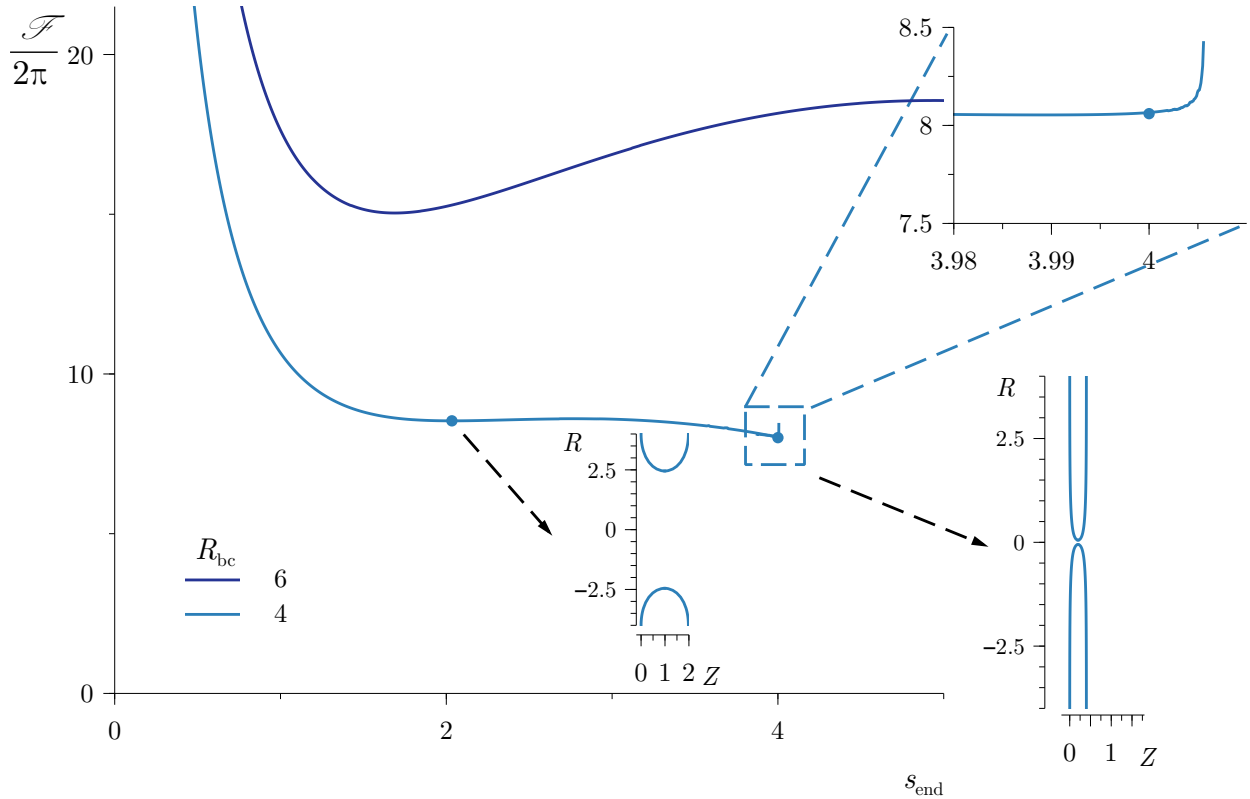

Figure 3. Dimensionless free energy $\mathscr{F}$ from Eq. (6) as a function of the arc length s_{end} for different values of the radial boundary size R_{bc}. The insets show shapes of the neck for $R_{\mathrm{bc}} = 4$ and two different values of s_{end}, corresponding to two local minima. The zoomed-in region depicts the sudden increase of free energy as the neck narrows.

$\tilde{\mathscr{F}}_{\mathrm{f}}$ [2–8, 11, 12]:

$$\tilde{\mathscr{F}} = \tilde{\mathscr{F}}_{\mathrm{m}} + \tilde{\mathscr{F}}_{\mathrm{p}} + \tilde{\mathscr{F}}_{\mathrm{f}} = \int_{\tilde{A}} \mathrm{d}\tilde{A} \left[\frac{\kappa}{2} (2\tilde{H})^2 + \sigma \right] + \int_{\tilde{V}} \mathrm{d}\tilde{V} \Delta\tilde{p} - \tilde{f} L, \tag{6}$$

where $\Delta\tilde{p} = p_{\mathrm{cyto}} - p_{\mathrm{peri}}$, $\tilde{A}$ is the area of the membrane neck, and $\tilde{V}$ is the volume inside the neck.

For axisymmetric surfaces, it proves convenient to describe the surface in terms of the angle $\theta(s)$ between the contour and the ordinate axis, as parametrized by the arclength s (see sketch in Fig. 1c). To non-dimensionalize Eq. (6), we again introduce the natural length scale $R_{\mathrm{c}} = \sqrt{\kappa/(2\gamma)}$ as the characteristic length. The definition of the radial $R(s)$ and axial $Z(s)$ coordinates, and the first variation of Eq. (6) yield the following nonlinear boundary-value problem [11, 13, 14]

$$R' = \cos\theta, \tag{7a}$$

$$Z' = -\sin\theta, \tag{7b}$$

$$\theta'' = -\frac{1}{2}(\theta')^2 \tan\theta - \frac{\cos\theta}{R}\theta' + \frac{\cos^2\theta + 1}{2R^2}\tan\theta + \frac{1}{2}\tan\theta + \frac{\Delta p R}{4\cos\theta} - \frac{f}{R\cos\theta}, \tag{7c}$$

where derivatives are with respect to contour length s, $\Delta p = \Delta\tilde{p} R_{\mathrm{c}}/\gamma$, and $f = \tilde{f}/(4\pi\gamma R_{\mathrm{c}})$. Concerning the boundary conditions, we impose $R(s = s_{\mathrm{end}}) = R_{\mathrm{bc}}$, $Z(s = s_{\mathrm{end}}) = 0$, $\theta(s = s_{\mathrm{end}}) = 0$, and $\theta(s = 0) = \pi/2$. The dimensionless free energy of the system is computed as

$$\frac{\mathscr{F}}{2\pi} = \int_A \mathrm{d}A[(2H)^2 + 1] + \frac{1}{2}\int_V \mathrm{d}V \Delta p - 2f\mathscr{L}, \tag{8}$$

where $\mathscr{L} = L/R_{\mathrm{c}}$. The system of differential equations (7a)–(7c) is solved using the Matlab® built-in boundary-value problem solver `bvp4c` [15, 16].

Fig. 3 shows the dimensionless version of the free energy from Eq. (6), as a function of the arc length s_{end} for different values of the radial boundary size R_{bc} indicated in the legend. When $R_{\mathrm{bc}} \gtrsim 3$, the free energy exhibits two local minima. One of them corresponds to a relatively small value of s_{end}, where the minimum neck radius is large, i.e. the neck opens up. The other local minimum occurs at a larger value of s_{end} with a larger associated free energy, corresponding to a narrow neck.

Increasing the value of s_{end} beyond the latter local minimum increases the total free energy drastically due to a sharp increase of the bending energy, as shown for $R_{\mathrm{bc}} = 4$ (zoomed region in Fig. 3). When $R_{\mathrm{bc}} \lesssim 3$, the free energy only displays one local minimum, which corresponds to that of a narrow neck. Fig. 4 is obtained using the same values of the parameters as in Fig. 3, but displaying some of the multiple higher-energy branches arising for sufficiently large values of s_{end}.

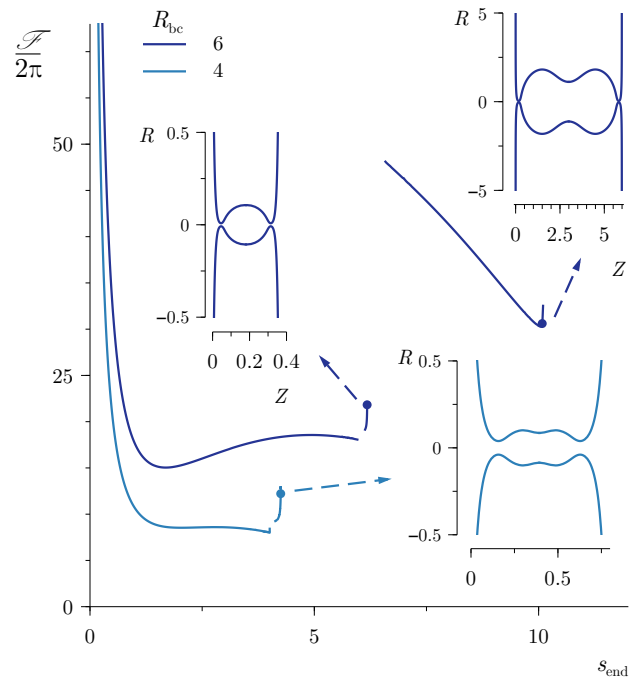

Figure 4. Same as in Fig. 3 but displaying some of the multiple branches arising for sufficiently large values of s_{end}.

Table I. Estimates of the physical and dimensionless parameters

Parameter	Value
κ	20 $k_B T$ [8]
γ	0.1–10 pN nm^{-1} [17–19]
L	40 nm
$\Delta\tilde{p}$	60 kPa [20]
$\tilde{f}$	50-100 pN [21, 22]
$R_c = \sqrt{\kappa/(2\gamma)}$	2–20 nm
L/R_c	9–90
$\Delta p = \Delta\tilde{p} R_c/\gamma$	0.012–12
$f = \tilde{f}/(4\pi\gamma R_c)$	0.4–4

Additionally, Fig. 5 shows the role of the pulling force f and the osmotic pressure difference Δp on the free energy and the shape of the membrane neck. Panel (a) depicts the dimensionless free energy $\mathscr{F}$ as a function of s_{end} for $f = 0$ and $f = 1.35$ (see Table I), and $\Delta p = 0$. The insets, showing the shape of the axisymmetric membrane neck at different values of s_{end}, demonstrate that, for the same values of R_{bc} and s_{end}, the pulling force tends to increase both the length of the neck and the minimum neck radius. Panel (b) displays the free energy with a non-zero value of the pulling force and the osmotic pressure difference, i.e. $f = 1.35$ and $\Delta p = 0.5$. As expected, incorporating a non-zero value of the osmotic pressure difference between the cytoplasm and the periplasm, slightly favors the narrowing of the membrane neck.

We now estimate some of the physical and dimensionless parameters used in the model and show that realistic values of the membrane tension and the osmotic pressure difference are able to sufficiently narrow the neck radius, to allow FisB proteins to interact and accumulate inside the neck. These estimates are shown in Table I. In particular, we consider a pulling force of $\tilde{f} \sim 50 - 100$ pN, which corresponds to the SpoIIIE maximum stall force [21, 22], and an osmotic pressure difference of $\Delta\tilde{p} \sim 60$ kPa, as estimated in Ref. [20]. Based on previous works [1, 23], we assume that FisB proteins are able to undergo homo-oligomerization in trans when the radius of the membrane neck is below ~ 10 nm, which is within the range of the estimated characteristic neck radius shown in Table I, $R_c = \sqrt{\kappa/(2\gamma)} \sim 2 - 20$ nm, where we have considered $\kappa \sim 20\, k_B T$ [8], and $\gamma \sim 0.1 - 10$ pN nm^{-1} [17–19] (see last section of this Appendix for an upper estimate of the membrane tension). According to the model, when $\Delta p = f = 0$, for the local minimum of the free energy $\mathscr{F}$ corresponding to the larger value of s_{end}, shown in Fig. 3, the dimensional minimum radius of the neck is $\tilde{R}_{\text{min}} \sim 0.1 - 1$ nm, which is significantly below the minimum radius required for FisB to interact. Moreover, the local free-energy minimum corresponding to a wider neck yields a minimum neck radius $\tilde{R}_{\text{min}} \sim 6.2 - 62$ nm, implying that, if membrane tension increases sufficiently, the neck radius for this local minimum can also be narrow enough for FisB to interact and accumulate inside the neck.

When $f = 1.35$ and $\Delta p = 0$, which corresponds to, for instance, $\gamma = 0.84$ pN nm^{-1} and $\tilde{f} \sim 100$ pN, we find $\tilde{R}_{\text{min}} \sim 4.5$ nm, corresponding to the membrane neck shown in the right bottom inset of Fig. 5(a). Hence, the action of a pulling force increases the radius of the neck, as compared to the case of $f = 0$ shown in Fig. 3 and 5(a). If we now consider the case of a non-zero value of the osmotic pressure difference, shown in Fig. 5(b), where we have used $f = 1.35$ and $\Delta p = 0.5$, corresponding to $\gamma \sim 0.84$ pN nm^{-1}, $\Delta\tilde{p} \sim 60$ kPa, and $\tilde{f} \sim 100$ pN, the minimum radius is $\tilde{R}_{\text{min}} \sim 4.1$ nm, thereby favoring the accumulation of FisB in the neck. Nonetheless, such osmotic pressure difference only reduces the minimum neck radius slightly, as we also observed in our highly simplified model shown in Fig. 2(b).

FLUX OF LIPIDS

To estimate the membrane tension difference between the two ends of the neck that would drive a flux of lipids from the mother cell to the forespore of $\sim 10^3$ lipids s^{-1} (see *Forespore inflation accompanies membrane fission* in the main text), we balance the force due to the membrane tension difference $\Delta\gamma$ and the drag force on a cylinder (i.e. the neck in our highly simplified model), translating parallel to its axis in an outer bath of viscosity μ,

$$2\pi R \Delta\gamma = \frac{4\pi\mu U L}{\ln(L/R) - 1/2}. \tag{9}$$

Considering that 1 lipid occupies ~ 0.7 nm^2 and assuming a neck radius of $R \sim 5$ nm, the required lipid velocity along the neck is $U \sim 22.3$ nm s^{-1}. Taking $L \sim 40$ nm and

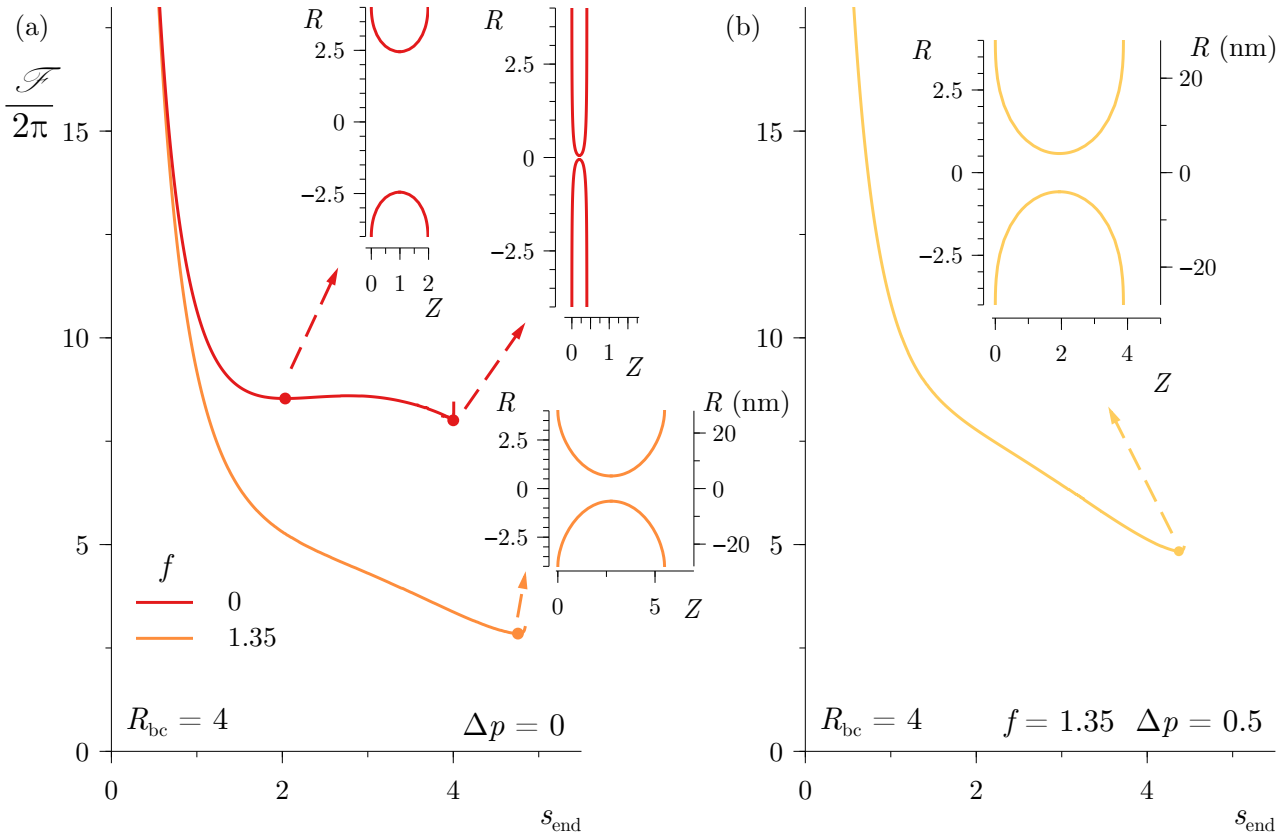

Figure 5. Dimensionless free energy $\mathscr{F}$ from Eq. (6) as a function of the arc length $s_{\rm end}$ for $R_{\rm bc} = 4$. Panel (a) shows $\mathscr{F}$ for two different values of the dimensionless pulling force f, with $\Delta p = 0$, and panel (b) shows the case $f = 1.35$, $\Delta p = 0.5$. The insets show the shapes of the neck for different values of $s_{\rm end}$ indicated with dots.

$\mu \sim 10^{-3}$ Pa s, the estimated membrane tension difference is $\Delta\gamma \sim 2.3 \times 10^{-7}$ pN nm^{-1}. Hence, a flux of $\sim 10^3$ lipids s^{-1} would require a relatively small excess membrane tension in the forespore engulfing membrane compared to the mother cell membrane, which we assume is of the same order as the estimate in Table I [17–19]. So in the absence of an accumulation of FisB in the neck that would slow lipid flow, a flux of lipids in the neck could readily provide $\sim 10^3$ lipids s^{-1} to the forespore membranes.

COMPARING THE STALL FORCE OF SPOIIIE TO THE OSMOTIC PRESSURE DIFFERENCE

Here we analyze how the osmotic pressure difference between the mother cell and the forespore compares to the stall/disassembly force of SpoIIIE [21, 22]. According to Ref. [20], the excess pressure in the forespore is of the order of 60 kPa, which can be related to a salt concentration difference $\Delta\rho$ between the mother cell and the forespore via $\Delta P = N_{\rm A} k_{\rm B} T \Delta\rho$, yielding $\Delta\rho \sim 25$ mM. Taking the salt concentration in the mother cell to be $\rho_{\rm mc} \sim 200$ mM [24, 25], the salt concentration inside the forespore is $\rho_{\rm fs} \sim 225$ mM. We can now estimate the energy required to move one salt ion into the forespore as $E = k_{\rm B} T \log(\rho_{\rm fs}/\rho_{\rm mc}) \sim 2.23 k_{\rm B} T$. This estimate is of the same order as the energy available from SpoIIIE, which is its stall maximal force, ~ 50 pN [21, 22], multiplied by half the base spacing, i.e. ~ 0.17 nm, since each translocated base of DNA brings $\sim$2 counterions, which yields $E_{\rm SpoIIIE} \sim 2.1 k_{\rm B} T$. This near equality of energies suggests that SpoIIIE works near its stall force, by creating the highest pressure difference it can in the forespore.

Moreover, we can estimate the forespore membrane tension that would be required to balance this osmotic pressure difference (for this estimate, we neglect the possible role of the peptidoglycan surrounding the forespore in opposing this osmotic pressure difference). Assuming that the forespore is a sphere surrounded by two membranes, the equilibrium excess pressure is given by the Laplace law, $\Delta P = 4\gamma/R_{\rm fs}$. Taking $R_{\rm fs} \sim 400$ nm, we obtain $\gamma \sim 6$ pN nm^{-1}. According to Refs. [17, 19], the rupture tension of a lipid membrane is $\gamma_{\rm rup} \sim 20$ pN nm^{-1}. Nonetheless, as shown in Ref. [18], the membrane rupture tension depends on the application time of the tension, and it can be of the order of $\gamma_{\rm rup} \sim 2 - 30$ pN nm^{-1} when $t_{\rm app} \sim 4 - 0.01$ min. Altogether, we argue that forespore inflation can give rise to an increase of membrane

tension enough to narrow the neck below 10 nm (see Equilibrium shapes of the axisymmetric membrane neck). Moreover, given that the characteristic time scale of forespore inflation is $t \sim 1 - 10$ min, the increased membrane tension due to forespore inflation may contribute directly to membrane fission.

[1] A. Landajuela, M. Braun, C. D. A. Rodrigues, A. Martínez-Calvo, T. Doan, F. Horenkamp, A. Andronicos, V. Shteyn, N. D. Williams, C. Lin, N. S. Wingreen, D. Z. Rudner, and E. Karatekin, PLOS Biology **19**, 1 (2021).
[2] W. Helfrich, Z. Naturforsch. C. **28**, 693 (1973).
[3] P. B. Canham, J. Theor. Bio. **26**, 61 (1970).
[4] O. Y. Zhong-Can and W. Helfrich, Phys. Rev. Lett. **59**, 2486 (1987).
[5] O.-Y. Zhong-Can and W. Helfrich, Phys. Rev. A **39**, 5280 (1989).
[6] U. Seifert and S. A. Langer, EPL **23**, 71 (1993).
[7] U. Seifert, Adv. Phys. **46**, 13 (1997).
[8] T. R. Powers, Rev. Mod. Phys. **82**, 1607 (2010).
[9] A. Karlsson, R. Karlsson, M. Karlsson, A. S. Cans, A. Strömberg, F. Ryttsén, and O. Orwar, Nature **409**, 150 (2001).
[10] P. Dommersnes, O. Orwar, F. Brochard-Wyart, and J. F. Joanny, EPL **70**, 271 (2005).
[11] I. Derényi, F. Jülicher, and J. Prost, Phys. Rev. Lett. **88**, 238101 (2002).
[12] T. R. Powers, G. Huber, and R. E. Goldstein, Phys. Rev. E. **65**, 041901 (2002).
[13] F. Jülicher and U. Seifert, Phys. Rev. E **49**, 4728 (1994).
[14] J. E. Hassinger, G. Oster, D. G. Drubin, and P. Rangamani, Proc. Nat. Acad. Sci. U.S.A **114**, E1118 (2017).
[15] J. Kierzenka and L. F. Shampine, ACM Trans. Math. Softw. **27**, 299 (2001).
[16] L. F. Shampine, J. Kierzenka, M. W. Reichelt, *et al.*, Tutorial notes **2000**, 1 (2000).
[17] D. Needham and R. S. Nunn, Biophys. J. **58**, 997 (1990).
[18] E. Evans, V. Heinrich, F. Ludwig, and W. Rawicz, Biophys. J. **85**, 2342 (2003).
[19] N. Ojkic, J. López-Garrido, K. Pogliano, and R. G. Endres, PLoS Comput. Biol. **10**, e1003912 (2014).
[20] J. Lopez-Garrido, N. Ojkic, K. Khanna, F. R. Wagner, E. Villa, R. G. Endres, and K. Pogliano, Cell **172**, 758 (2018).
[21] J.-F. Allemand and B. Maier, FEMS Microbiol. Rev. **33**, 593 (2009).
[22] N. Liu, G. Chistol, Y. Cui, and C. Bustamante, eLife **7**, e32354 (2018).
[23] S. Ovchinnikov, H. Park, N. Varghese, P.-S. Huang, G. A. Pavlopoulos, D. E. Kim, H. Kamisetty, N. C. Kyrpides, and D. Baker, Science **355**, 294 (2017).
[24] B. Schmidt-Nielsen, J. Exp. Zool. **194**, 207 (1975).
[25] F.-X. Theillet, A. Binolfi, T. Frembgen-Kesner, K. Hingorani, M. Sarkar, C. Kyne, C. Li, P. B. Crowley, L. Gierasch, G. J. Pielak, *et al.*, Chem. Rev. **114**, 6661 (2014).